Journal Pre-proof

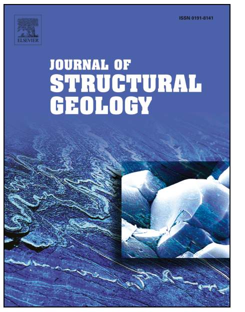

Damage zone heterogeneity on seismogenic faults in crystalline rock; a field study of the Borrego Fault, Baja California

Giles A. Ostermeijer, Thomas M. Mitchell, Franciscus M. Aben, Matthew T. Dorsey, John Browning, Thomas K. Rockwell, John M. Fletcher, Francis Ostermeijer

PII: S0191-8141(19)30323-2

DOI: https://doi.org/10.1016/j.jsg.2020.104016

Reference: SG 104016

To appear in: *Journal of Structural Geology*

Received Date: 1 August 2019

Revised Date: 12 February 2020

Accepted Date: 13 February 2020

Please cite this article as: Ostermeijer, G.A., Mitchell, T.M., Aben, F.M., Dorsey, M.T., Browning, J., Rockwell, T.K., Fletcher, J.M., Ostermeijer, F., Damage zone heterogeneity on seismogenic faults in crystalline rock; a field study of the Borrego Fault, Baja California, *Journal of Structural Geology* (2020), doi: https://doi.org/10.1016/j.jsg.2020.104016.

Giles A. Ostermeijer: Conceptualization, Methodology, Validation, Formal analysis, Investigation, Writing - All versions, Visualization, Project administration, Funding acquisition. **Thomas M. Mitchell:** Conceptualization, Supervision, Funding acquisition, Writing - Review & Editing. **Franciscus M. Aben:** Software, Investigation, Writing - All versions. **Matthew T. Dorsey:** Investigation, Writing - Review & Editing. **John Browning:** Investigation, Writing - Review & Editing. **Tom K. Rockwell:** Resources, Writing - Review & Editing, Supervision. **John M. Fletcher:** Resources, Writing - Original Draft, Supervision. **Francis J. Ostermeijer:** Formal analysis, Resources, Data Curation.

Damage Zone Heterogeneity on Seismogenic Faults in Crystalline Rock; a Field Study of the Borrego Fault, Baja California.

*Giles A. Ostermeijer[a] giles.ostermeijer.15@ucl.ac.uk

Thomas M. Mitchell[a] tom.mitchell@ucl.ac.uk

Franciscus M. Aben[a] f.aben@ucl.ac.uk

Matthew T. Dorsey[b,1] dorsey@tamu.edu

John Browning[a,2] jbrowning@ing.puc.cl

Thomas K. Rockwell[b] trockwell@sdsu.edu

John M. Fletcher[c] jfletche@cicese.mx

Francis Ostermeijer[d] francis.ostermeijer@vu.nl

* : corresponding author, email: giles.ostermeijer.15@ucl.ac.uk

[a] *University College London, Department of Earth Sciences, Gower Street, London, WC1E 6BT, UK*

[b] *San Diego State University, Department of Geological Sciences, MC-1020, 5500 Campanile Dr., San Diego, CA 92182-1020, USA*

[c] *División de Ciencias de la Tierra, Centro de Investigación Científica y de Educación Superior de Ensenada, Ensenada, Mexico*

[d] *Vrije Universiteit Amsterdam, School of Business and Economics, Amsterdam, Netherlands*

[1] now at: *Texas A&M University, College Station, TX 77843, USA*

[2] now at: *Department of Mining Engineering and Department of Structural and Geotechnical Engineering, Pontificia Universidad Católica de Chile, Santiago, Chile*

Keywords: damage zone; fault zone structure; fractures; damage heterogeneity; fracture density

Abstract

Complex fracture damage around large faults is often simplified to fit exponential or power law decay in fracture density with distance from the fault. Noise in these datasets is attributed to large subsidiary faults or random natural variation. Through a field study of the Borrego Fault (Baja California) damage zone, combining mm-resolution structural mapping and point sampling, we show that such variations are the expression of systematic damage heterogeneity. The oblique-slip Borrego Fault comprises NW and SE segments that ruptured during the Mw7.2 2010 El Mayor-Cucapah earthquake. Measurements of fracture density along eight linear fault-perpendicular transects and from a high-resolution 68 m^2 structural map display a power law decay and define footwall damage zone widths of ~85 m and ~120 m for the NW and SE segments respectively. Variance in fracture density decays with distance following an inverse exponential relationship, to background variance at ~16 m. Spatial analysis of the high-resolution fracture map reveals a patchy distribution of high- and low-intensity clusters at metre- and decimetre-scales. We attribute high-intensity clusters at these scales to local complexity caused by interactions between minor subsidiary faults (10^1 m length and 10^{-2}-10^{-1} m displacement). Fracture density differences between high- and low-intensity clusters decrease with distance from the fault, demonstrating a systematic change in outcrop-scale damage heterogeneity. Based on these observations we present a revised model for damage zone growth including growth of heterogeneity.

Abbreviations used in this paper:

DZW – damage zone width

BFD – background fracture damage

1 Introduction

In crustal fault zones, dynamic rupture and fault slip is typically hosted within a narrow fault core, surrounded by a fracture damage zone (Figure 1) of up to 100s of metres in width (e.g. Ben-Zion and Sammis, 2003; Chester and Chester, 2000; Chester and Logan, 1986; Rowe et al., 2013; Savage and Brodsky, 2011; Scholz, 1987; Sibson, 1986, 2003). This damage is accrued by a combination of aseismic/quasi-static (e.g. Chester and Chester, 2000; Childs et al., 2009; Cowie and Scholz, 1992; Faulkner et al., 2011) and coseismic processes (e.g. Aben et al., 2016; Ben-Zion and Ampuero, 2009; Johri et al., 2014a; Okubo et al., 2019; Rempe et al., 2013; Rice et al., 2005; Sagy and Korngreen, 2012; Xu et al., 2012). Fractured rock can have significantly different mechanical and hydraulic properties to intact rock, and so the damage zone plays a fundamental role in crustal fluid flow and the mechanics of faulting and earthquakes. Firstly, damaged fault rocks are generally more permeable with higher surface area than intact rocks, and hence play a key role in the migration of fluids and precipitation of minerals in and around fault zones over the seismic cycle (e.g. Evans et al., 1997; Hennings et al., 2012; Lawther et al., 2016; Lockner et al., 2000; Seront et al., 1998; Sibson, 1994). Secondly, damaged rocks have reduced elastic moduli, cohesion and yield strength (e.g. Bruhn et al., 1994; Callahan et al., 2019; Faulkner et al., 2006; Griffith et al., 2012; Griffith et al., 2009; Walsh, 1965), resulting in reduced elastic wave velocity, which can cause attenuation and potentially non-linear wave propagation effects during ruptures (e.g. Wu et al., 2009). The amount and spatial variation of these reductions can directly modify rupture dynamics/style/shape (e.g. Cappa et al., 2014; Dunham et al., 2011; Huang and Ampuero, 2011; Okubo et al., 2019), and lead to the generation of slip pulses that can accelerate the transition to supershear rupture (e.g. Harris and Day, 1997; Huang and Ampuero, 2011). Significant velocity reductions within a fault zone results in the structures trapping seismic waves that can continuously perturb stresses on the fault during earthquakes. Finally, the dynamic generation of damage as the earthquake rupture propagates can itself influence the dynamics of rupture propagation. This can be done by increasing energy dissipation (e.g. Andrews, 2005), modulating the rupture velocity (Cappa, 2011; Huang et al., 2014; Thomas et al., 2017) and modifying the size of the earthquake, changing the efficiency of weakening mechanisms such as thermal pressurisation of pore fluids (e.g. Brantut and Mitchell, 2018; Noda and Lapusta, 2013), and even generating additional seismic waves (e.g. Ben-Zion and Ampuero, 2009).

With increasing displacement and fault maturity, fracture damage zones increase in both width and complexity (Figure 1). This increased width and complexity is due to overprinting of incremental fracture damage, which leads to heterogeneity in off-fault damage structures. Furthermore, strong rock-type dependencies (Bistacchi et al., 2010; Loveless et al., 2011; O'Hara et al., 2017) and the influence of pre-existing structures (e.g. Brogi, 2011; Myers and Aydin, 2004) can also lead to spatial heterogeneities in damage formation. Heterogeneous damage patterns lead to heterogeneous mechanical and hydraulic properties of the same scale and distribution. Thus, quantifying damage heterogeneity is fundamental in understanding the complex effects and feedbacks on earthquake processes. To date, most observations of damage heterogeneity are limited to qualitative description only (Caine et al., 2010; Gudmundsson et al., 2002; Gudmundsson et al., 2010).

Most classical fundamental studies of fault zone damage were based on detailed qualitative structural geology techniques (e.g. Crider and Peacock, 2004; Price and Cosgrove, 1990). This approach identified three broad zones of damage, based on the type, intensity, and extent of fracturing; tip, wall, and interaction damage (Kim et al., 2000; Kim et al., 2003; Kim et al., 2004; Peacock et al., 2016) (Figure 1a). Initially, interaction and tip zones show the most complex and intense damage, while wall zones develop more complexity as the fault grows through cumulative slip (Kim and Sanderson, 2008; Madariaga, 1983; Rousseau and Rosakis, 2003). More recent quantitative approaches of damage analysis have been developed in order to answer fundamental questions on the seismic cycle, such as fault strength, fluid flow properties and rupture dynamics. To do so, it was necessary to simplify the complex off-fault damage so that usable mathematical expressions describing the spatial and temporal distribution of damage could be derived (e.g. Chester et al., 2005; Choi et al., 2016; Savage and Brodsky, 2011; Shipton and Cowie, 2003) (e.g.

Figure 1d,e). For simplicity, we apply the following damage terminologies (adopted from Shipton and Cowie (2001)) for fault/fracture length scales relative to the main fault, where main fault length is >km: (1) *Macro-damage*, 1-3 orders of magnitude smaller [10^1-10^3 m]; (2) *Meso-damage*, 3-5 orders of magnitude smaller [10^{-2}-10^1 m]; and (3) *Micro-damage*, >5 orders of magnitude smaller [<10^{-2} m]. Results from studies measuring micro- and meso-fracture densities on fault perpendicular transects show that across-fault 1-D damage profiles can be simplified to fit either an exponential decay model (log-normal linear regression) (Mitchell and Faulkner, 2009), or a power law decay model (log-log linear regression) (Johri et al., 2014b; O'Hara et al., 2017; Savage and Brodsky, 2011). These quantitative studies do not address the patterns in damage heterogeneity observed in many of the datasets, and although there are many field studies of off-fault damage, it is problematic to compare datasets due to a lack of consistency in the data sampling techniques, the scales at which damage is measured (micro, meso, and macro), terminology and nomenclature, lithological and tectonic differences, and variations in analytical approach (Choi et al., 2016).

[Figure 1 here]

Despite heterogeneous damage distributions within fault zones having been shown to theoretically have significant effects on earthquake ruptures (e.g. Cappa, 2011), our understanding of the distribution of off-fault damage heterogeneity and how it scales with increasing fault maturity is surprisingly poor. This is in part due to little being known about the relative contributions of quasi-static and dynamically induced fractures in seismic fault zones, and how this damage evolves cumulatively in time and space. To complicate matters, with increased pressure and temperature at depth, the structure, mechanical, and hydraulic characteristics of a fault zone are subject to constant change (e.g. healing and/or sealing) during the seismic cycle as the fault evolves (e.g. Eichhubl et al., 2009; Faulkner et al., 2010; Rempe et al., 2018; Williams et al., 2017).

In this study we aim to address the data gap between qualitative and quantitative descriptions of meso-scale (10^{-2}-10^1 m long faults/fractures) fault damage heterogeneity by performing a comprehensive high-resolution field study and analysis of outcrop-scale fracture patterns along the km-scale active Borrego Fault, Baja California. While most existing studies are limited to measuring damage trends on one or two fault perpendicular transects, we collected an extensive along-strike dataset of eight transects and made a mm-scale resolution 2D fracture map from a damage zone outcrop on a river bed pavement with 100% exposure. This dataset allows us to quantify the distribution of heterogeneities at decimetre to decametre scales, providing a detailed characterisation of the distribution of meso-scale damage around large seismogenic faults. The 2D damage map presented here may offer improved insights into the cumulative growth of off-fault damage, and how this feeds back into the faulting and earthquake process. This dataset also allows the critical comparison of different fracture sampling techniques, and the impact of sampling resolution/density on quantifying fault damage.

2 Geological setting

For this study we selected the Borrego Fault, an active, seismogenic fault in the Sierra Cucapah range of Northern Baja California, due to having a monolithic igneous basement, a well-documented seismic record, access to outcrops, and known coseismic damage following a Mw 7.2 earthquake in 2010 (Teran et al., 2015). This fault has 3-8 km of displacement (Barnard, 1969), and therefore we consider it to be of intermediate maturity relative to larger crustal scale faults such as the San Andreas. Syn-kinematic deformation was limited to relatively shallow conditions, occurring at depths less than 2 km (Fletcher et al., 2014) and temperatures of less than 200°C (Dorsey et al., IN PREP).

2.1 *Local geology and morphology of the Borrego fault, Baja California*

The Borrego Fault is located on the western side of the Sierra Cucapah mountain range in Baja California, Mexico (Figure 2a). The Sierra Cucapah are a narrow belt of mountains in an uplifted horst block striking NW-SE, exposing the predominantly crystalline basement rocks, bound by the Cerro Prieto and Laguna Salada sedimentary basins to the east and west. Located on the western margin of the Gulf of California-Salton Trough province, the area is part of the Southern San Andreas tectonic regime, currently undergoing right-lateral transtensional regional displacement (Dorsey and Umhoefer, 2012; Lizarralde et al., 2007; Umhoefer, 2011; Withjack and Jamison, 1986). The range is dissected by a complex network of interconnected faults, dominated by large, km-scale faults oriented parallel to the range, with displacements of 100’s to 1000’s of metres. The 2010 Mw7.2 El Mayor Cucapah earthquake ruptured sections of most major faults in the Sierra Cucapah, including portions of the Borrego Fault (Fletcher et al., 2014; Teran et al., 2015).

[Figure 2 here]

Basement rocks exposed in the Sierra Cucapah predominantly consist of medium-coarse grained Cretaceous granitoid plutons and Palaeozoic metasediments (mainly gneiss and marble), which are juxtaposed with Miocene and younger fanglomeratic, deltaic, and volcanic units (Barnard, 1969). Most of the plutonic rocks show a pervasive weak deuteric alteration that is characterised by a chlorite-epidote-titanite assemblage (Dorsey et al., IN PREP). Moderate alteration arises from circulation of Na- and Mg-rich hydrothermal brine (Dorsey et al., IN PREP), and is spatially related to faults in the region.

The Borrego Fault is a NE dipping structure with a 28-31 km surface trace, directly adjacent to the west-dipping, range-bounding Laguna Salada Fault. The bedrock hosting the Borrego Fault consists of tonalite and melanocratic phase granodiorite with a grainsize between 2-10 mm. These rocks outcrop extensively in the footwall of the fault, and are well exposed in deeply incised drainage channels that extend up to 100 m away from the fault core. Hanging-wall rocks are comprised mainly of Pliocene-Quaternary fanglomerate and alluvial sediments overlying metasedimentary and volcanic units, hosted in a long, narrow graben bound to the NE by the Cascabel Fault. The Cascabel Fault dips steeply towards, and is intersected by the Borrego Fault at a depth of 1-2 km.

Palaeoseismic studies revealed evidence of four surface ruptures similar to the 2010 El Mayor-Cucapah earthquake with an average recurrence interval of ~10 ka (Hernandez et al., 2013). The fault morphology is relatively complex, with two distinctly different segments separated by a northward bend about a third of the way along the fault, starting in the North (Figure 2b, label *(3)*). These segments will be referred to from here on as the NW and SE segments, with the splay roughly half way along the bend as the dividing point. Further information on regional and local geology, and morphology of the Borrego fault, is included in SI 1.

2.1.1 SE segment

The predominantly linear SE segment extends about 18 km southeast of the bend where it terminates on the Laguna Salada Fault. The segment dips between 40-65° and is characterised by shear structures and high strain material, hosted within a diffuse array of scarps and splays. This represents a multi-strand fault core that at its widest is around 50 m thick (Teran et al., 2015) (Figure 3). The segment hosts 6-8 km of displacement (Fletcher et al., 2020), with a lateral to vertical ratio of approximately 3:1.

2.1.2 NW segment

The NW segment consists of two strands that split at the apex of the dividing bend: A steep strand striking parallel to the SE segment, and a more gently dipping strand oriented towards the west (labels *(1)* and *(2)* in Figure 2b respectively). The total offset is distributed almost equally between the two strands (Fletcher et al., 2020) but the steep strand is more favourably oriented for accommodating lateral displacement (L:V ratio of ~2 (Fletcher et al., 2014)). A single core, formed of clay gouge, cataclasite bands, and ribbons of entrained hanging-wall material, is found along much of the steep strand. The core is up to 1.5 m thick and is at places dissected and buried in the hanging-wall by more recent ruptures. In this study we only consider the steep strand in future reference to the NW segment.

In the footwall along the NW segment, immediately adjacent to the core, we observe intensely shattered rock, characterised by a gritty to powdery texture when handled. This material comprises up to 70% of the rock mass adjacent to the core, reducing to 20-30% after 0.2-1 m, and negligible volumes after 2-3 m. Pods or lenses of intact material, 3-20 cm in size, are found throughout this part of the inner damage zone and progressively increase in both abundance and size with distance from the core. Preservation of the original rock fabric and grain boundaries suggest that most of this volume accommodates only small amounts of shear which is limited to narrow, crosscutting bands of ultracataclasite and gouge. The rock is characterised by predominantly in-situ sub-grain shattering, resulting in a grainsize reduction to silt/fine sand. This severe reduction of grainsize and similarity to textures described by Dor et al. (2006) leads us to interpret this as a zone of partial pulverisation (e.g. Aben et al., 2017; Dor et al., 2006; Mitchell et al., 2011; Reches and Dewers, 2005; Wechsler et al., 2011). We differentiate pulverisation from grus by the lack of significant weathering products, its structural context, and substantial grainsize reduction. Pulverisation is rarely found in the footwall of the damage zone along the SE segment of the fault, but occurs more commonly in less sheared pods within the wide multi-core zone. This partially pulverised zone is the subject of additional study.

2.2 *Field sites*

The field sites consist of eight transects and a bedrock pavement, all located in the exposed footwall (Figure 3). We quantified meso-fractures (cm to tens of m long) along the transects, and studied the meso-fracture distribution in 2D at the bedrock pavement. The inclusion of transect data allows direct comparisons to be made with observations and methodologies from existing literature, while also providing context to the unique dataset obtained from the 2D pavement.

[Figure 3 here]

2.2.1 Linear transects (x8)

Four transects were selected on each fault segment. Along the NW segment, the transects were spaced at 100-200 m intervals between 1-2 km NW of the dividing bend. On the SE segment, one transect was located within the dividing bend, and three were distributed evenly between 300 m and 1500 m along the SE section (Figure 3). All transects were located in drainage channels that were oriented roughly fault-perpendicular, and provide semi-continuous linear outcrops that extend upslope away from the fault.

2.2.2 Pavement

A kilometre NW of the dividing bend along the NW segment, within the channel floor of a dry 5-6 m wide arroyo, a bedrock pavement provided continuous exposure from the 2010 fault rupture surface up to 20 m into the footwall damage zone. Downward displacement of the hanging-wall during the 2010 rupture produced a 1.7 m high dam in the downstream portion of the drainage arroyo. Following heavy storms in 2012-2013, the uplifted footwall was stripped of overlying sediment to reveal a near horizontal pavement of basement tonalite (Figure 4).

The exposed rock on the pavement is composed of an undulating fault core between 0.5-1.3 m thick and an intensely fractured tonalite comprising the footwall damage zone. Weak to moderate alteration in the damage zone is evidenced by a slight green colouration of the rock, but original rock fabric and texture are preserved. The fault core is formed of red-brown gouge with a distinct shear fabric and incorporated hanging-wall clasts. These clasts are mainly composed of fragments, lenses, and ribbons of Palaeozoic metacarbonates that have been partially assimilated into the gouge.

[Figure 4 here]

3 Methodologies

3.1 *1D meso-fracture transects*

There have been several methods used for the collection of in-situ meso-fracture data from transects oriented roughly perpendicular to studied faults. They can be separated into three groups: (1) Continuous 1D scanlines (e.g. Berg and Skar, 2005; Brogi, 2008; Choi et al., 2016; Micarelli et al., 2006b; O'Hara et al., 2017); (2) point location line sampling (e.g. Mitchell and Faulkner, 2009); and (3) point location area sampling (Micarelli et al., 2006b).

We could not perform the more robust continuous 1D scanline methodology suggested by Choi et al. (2016) for several reasons: (1) the irregular, blocky exposure that is found along the Borrego Fault; (2) the relatively high fracture density; (3) the need for a vertical measurement dimension to capture sub-horizontal fractures, and (4) time limitations in the field. Instead, we collected meso-fracture data following a modified version of the line sampling method for measuring discontinuity spacing/frequency (also referred to as line density or line counting method – e.g. Faulkner et al. (2010); Wilson et al. (2003)), and as also described in the 'Suggested Methods' published by the ISRM Commission on Standardization of Laboratory and Field Tests (ISRM, 1978). We recorded the number of fractures spanning more than one grain (>2 cm long) that intersect two perpendicular 30 cm rulers (horizontal ~ fault perpendicular, and vertical), to obtain the linear density of fractures (number of fractures per metre). Measurements were taken from vertical exposures along the steep sides of the drainage channels where outcrop quality was best. At each sample location along a transect (see Figure 5), we recorded three non-overlapping measurements to capture the range of fracture densities more accurately.

For better quality results, higher sampling coverage should coincide with the greatest expected rate of change in the damage zone fracture density profile. Hence, if the Borrego Fault displays exponential or power law decay, in meso-fracture density, similar to other faults, then sampling frequencies should be highest where the most rapid decay in density is expected. We assumed an exponential decay model for meso-scale fracture damage in crystalline rock (Mitchell and Faulkner, 2009) and estimated the damage zone width (DZW) of the Borrego Fault by combining the linear damage zone width vs. fault displacement relationship shown by Savage and Brodsky (2011) and Choi et al. (2016) with data from a preliminary damage zone survey. This estimate yielded a DZW of 30-70 m, with the most rapid decay in fracture density occurring within 20 m of the fault core, on which we designed the sampling frequency (Figure 5). Note that, in practice, measurements were also dependent on outcrop quality and exposure. All distances from the fault were corrected for topographic effects and fault dip.

Using a power law decay model, instead of the exponential decay model that we used, to design a sampling frequency would increase the estimated DZW but push the rapid decay in fracture density closer to the fault core. Hence, the exponential model produced a more conservative sampling frequency (i.e. higher sampling densities extending further from the fault). If the Borrego Fault does not display either of these two decay models, the higher sampling density close to the fault, that we performed, should not appreciably skew the data.

[Figure 5 here]

3.2 *2D pavement*

For the river bed pavement, we generated a 2D dataset through continuous area sampling and by digitising the entire visible fracture network. This was done by physically overlaying a m^2-grid onto the outcrop, taking photos of each square metre with a hand-held DSLR (2 mm pixel size), tracing fractures onto the photos and then stitching the entire grid together in Adobe Illustrator (Details on image capture and processing are outlined in SI 2.2). We analysed the digital fracture network using both 1D and 2D techniques.

For 1D analysis, we generated seven 16.5 m long and two 9 m long transects through the digital fracture network by overlaying a grid of 50x50 cm cells to give a continuous string of box counts. From the individual grid cells, we extracted data on fracture density/intensity, strike orientations, and fracture length distributions. We then performed standard statistical analysis on the fracture intensity and density data, including variance (S^2), standard deviation (S), and semi-interquartile range (SIR) as a function of distance from the fault. S^2, S, and SIR indicate the spread of data at any given distance, assuming that the mean trend is an accurate representation of the overall damage profile. SIR removes the influence of outliers in the dataset but requires a large dataset as the sample size is reduced after the removal of data at the extremes of the distribution. To analyse fracture spacing patterns, we generated additional scanlines, from the digital fracture network, at 10 cm intervals in four orientations (fault parallel, fault perpendicular, and two oblique sets at 45° to the fault). The 1D analysis results were compared with those from the 1D transects to confirm the representativeness of the pavement for the entire Borrego Fault damage zone, and hence also the representativeness of the 2D analysis.

2D analysis was performed using the Fracture Intensity Map and Fracture Orientation functions in FracPaQ, a MATLAB™ toolbox designed for quantifying fracture patterns. A complete description of the FracPaQ toolbox and where to access it is outlined in Healy et al. (2017).

3.3 *Accounting for potential sources of error*

3.3.1 Background fracture density (BFD)

We measured background fracture density at various locations between 150-1000 m from the fault in areas considered to be free from the influence of faulting. At these localities we took photos and performed the line sampling technique. The measured background fracture densities in the SE horst block generally ranged between 9-35 m^{-1} (fractures/metre) but with sporadic extremes as low as 3 m^{-1} and as high as 45 m^{-1}. We found a higher background fracture density, ranging between 12-38 m^{-1}, in the NW footwall block (Figure 3), with similar extremes (3-45 m^{-1}) in small patches. The average BFD, calculated from frequency distributions and using one standard deviation for the uncertainty, is 24 m^{-1} [20-29 m^{-1}] and 27 m^{-1} [23-30 m^{-1}] for the SE and NW horst blocks respectively. Variance (S^2) in BFD measurements is 5.5 m^{-2} for the SE block and 4.7 m^{-2} for the NW block.

BFD for the 2D analysis was obtained using box counts from the photos taken at the same resolution as the photos of the pavement. The measured number of fractures, which exhibited no clear preferred orientation, ranged between 20-120 m^{-2}, with an average and uncertainty of 61 m^{-2} [45-80 m^{-2}].

3.3.2 The influence of major subsidiary faults

We recorded the location of major faults, whether predating or subsidiary to the main Borrego structure, on every transect of both segments. We define 'major faults' as structures containing cataclasite or gouge zones, visibly increased damage intensity along most, or all, of their length, and greater than 20 cm displacement (with some exceeding 10^1 m). Subsidiary fault displacement was determined using offset markers such as quartz veins, cross-cutting shear bands (Figure 4b), or patches of compositional variation. On faults where the precise displacement was difficult to determine, we used observable fault length as a proxy (Dawers and Anders, 1995; Grasemann et al., 2011). Major subsidiary faults were recorded because they significantly impact fracture density. When sampling within their range of influence – 0.2-5 m depending on displacement – we noted peaks in fracture density above the general trend (Figure 6a,b). These faults are thus sufficiently large to have accrued their own local meso-damage zones (e.g. Mitchell and Faulkner, 2009). We separated the measurements affected by the increased damage around major subsidiary faults so that the resulting trend provides the closest approximation to a meso-damage zone associated to the Borrego fault only.

Faults containing a core (often poorly developed), non-continuous/limited wall damage, and displacement of only a few centimetres (generally <20 cm) are considered minor subsidiary faults, and we do not separate measurements taken near these faults. Note, we differentiate between major and minor faults by the presence of a continuous damage zone rather than a precise displacement cut-off. All of the subsidiary faults observed on the pavement were minor (Figure 4b, Figure 7b).

4 Quantitative meso-damage results

The results from the 1D transect study provide an overview of the damage zone surrounding the Borrego Fault, giving spatial context to the pavement. This dataset is similar to previous damage zone studies, and so we can compare it to both historic datasets, and the 2D study described in section 4.2. From the transect data we also identify key questions that are addressed more thoroughly using the high-resolution 2D dataset.

While most meso-fractures display opening mode characteristics (Figure 4c,d), many of the longer fractures (>m) display evidence of shear displacement with cataclastic fill (Figure 4b,c). Very few of the meso-fractures in the damage zone along the Borrego Fault are infilled by minerals. Those fractures which are infilled are primarily sealed with green chlorite, and cm wide alteration halos are observed along some of the larger fractures.

4.1 *Transect data*

We observe similar maximum meso-fracture densities of 70-81 m^{-1} within the first 5 m of the fault for all transects along the SE and NW fault segments, which is 2.5-3 times higher than the background fracture density (Table 1). For transects where measurements commenced directly against the fault core, we observed maximum fracture densities at 3 m from the core for the NW transects, but adjacent to the core for the SE transects (Table 1). This *'shifted maxima'* is likely caused by a bias arising from the partially pulverised zone along the NW segment. Partially pulverised rock within 0-3 m (occasionally extending up to 5 m) obscures the observation of meso-fractures (>2 cm in length), and thus reduces meso-fracture counts. Furthermore, our observations suggest that non-pulverised blocks within the pulverised zone have a notably lower damage intensity than expected. Therefore, we elected to ignore data from the partially pulverised zone for the regression models of the NW segment. The SE segment lacks pulverisation in the damage zone, and damage maxima were measured adjacent to the fault core.

[Insert Table 1 here]

Damage density and rate of damage decay clearly both decrease with distance from the fault (Figure 6a,b). The spread of densities also significantly narrow, with distance from the fault core, resulting in a wedge-shaped distribution where the largest span is close to the core. The distribution tapers with distance from the core towards the background variance (Figure 6a,b). We used variance (S^2) to quantify the spread at each distance interval from the fault core to quantitatively describe this wedge-shaped distribution. By doing so, we identify a clear decrease in the along-strike variance away from the core (Figure 6c,d). A prominent transition occurs along both segments at 10-15 m from the fault, separating an inner zone of high and irregular variance from an outer zone of uniform and low variance that extends into the undamaged host rock. There is no statistical relationship between the number of samples at a given distance from the fault and the variance, indicating that the observed trend is likely not caused by bias in the sample number. An anomalously high value, at 90 m on the SE segment, may be caused by a nearby major subsidiary fault.

[Figure 6 here]

We averaged the meso-fracture densities from the four transects on each segment to produce a representative trend. In natural logarithmic space, fracture density versus distance from the fault core is revealed as a linear trend (Figure 6e,f), suggesting power law decay with distance:

$$y = ax^n, \quad (1)$$

where y is the fracture density, a is a fault constant, x is the distance from the fault core, and n is the slope coefficient, which is negative due to the inverse x-y relationship. We obtained the best fit for a power law trend for each fault segment (Table 1). The damage zone width (DZW) for each fault segment was then estimated from the intersection of the regression-line with the average background damage. Uncertainties were derived using the 95% confidence of the trend and the errors on the average background density (modified from Knott et al. (1996)). We obtained a footwall DZW of 82 m [51-170 m] for the NW strand, and 122 m [37-519 m] for the SE strand. Note an exponential model fits the data better for some transects, but for most, including the NW and SE combined and averaged datasets, a power law model provided a better fit (for individual transect results see SI 3.4) and has more randomly distributed plot residuals (SI 3.5). A power law model also corresponds to elastic models of deformation produced from a point or line source, that suggest a power law decay in stresses with distance from the fault (Love, 1927).

The results of the transect study show that the pavement, which extends outward to ~20 m from the fault core, offers an observation window of approximately 11-38% of the total damage zone width, but covers 65-75% of the damage decay. In addition, the pavement covers the apparent high-low variance transition distance between 10-15 m from the fault (Figure 6c,d), allowing us to examine the characteristics of this zone in more detail.

4.2 *2D pavement data*

A total of 11,114 fractures were traced on the pavement over a 68 m^2 area (Figure 7). This covers two orders of magnitude of fracture lengths, from a minimum length of 2 cm to a maximum traceable length of 5 m, so that the traced elements are 4-6 orders of magnitude smaller than the Borrego Fault length. Fracture lengths follow a power law distribution between 0.2-2 m (Figure 8e). Smaller fractures (<0.2 m) were underrepresented due to intentional detection limits set by limiting magnification, as well as difficulties in identifying some small fractures, while observation of larger fractures (>2 m) were affected by outcrop scale (i.e. truncation of fractures extending past the edges of the sampling area).

[Figure 7 here]

We observe a counter-clockwise rotation of the dominant fracture orientation from fault sub-parallel within 1-2 m of the fault core, to around 35° after 10 m from the core (Figure 7d). Over the same length scale, we see a clear transition from a single dominant fracture set to two fracture sets. The fracture density maxima (around 500 m^{-2}) measured for each pavement transect (Table 2) are located between 1-2.5 m from the fault core. Similar to the NW 1D-transects, we attribute this shift to a bias caused by pulverisation, rather than a real reduction of fracture density within the initial 1-1.5 m. Therefore, we omit these values when calculating the DZW.

Minor outcrop-scale subsidiary faults offset smaller fractures by several centimetres, up to a maximum of 20 cm. It was not possible to determine the relative timing of individual minor subsidiary faults and so these offsets could not be used as displacement indicators. Several of the larger minor subsidiary faults displayed halos of alteration and thin strands of brown clay-gouge.

These zones of increased alteration may imply higher porosity linked to micro-fracture damage associated with the minor subsidiary faults. Based on these characteristics (measurable shear displacement and/or >2 mm thick cores), we identified and mapped the minor subsidiary faults on the pavement (Figure 7b).

4.2.1 1D transects from 2D dataset

Fracture density results from the 1D analysis derived from the pavement correspond well with the results from the larger scale transect study: we observe a similar tapering effect in scatter, and the power law regression for the average trend projects to intersect the background density at 90 m [44-258 m] (Figure 8a,b). The power law regression is justified by the goodness of fit (R^2, Table 2), plot residuals (SI 3.5), and the Breusch-Pagan statistical test, detailed in SI 3.6. Regression lines for individual transects intersect the average background density between 52-134 m, displaying 43-49% deviation from the averaged regression, and ~160% change between the smallest and largest DZW (Table 2). While the average values show little scatter around the regression (R^2 = 0.89), individual transects display significant scatter, with R^2 values ranging from 0.31-0.80.

[Insert Table 2 here]

Total fracture length and fracture density share the same inverse relationship with distance from the fault (Figure 8c). The ratio of the two indicates that fractures become longer with distance from the fault (Figure 8d), on average. The relative proportion of space between fractures within the 5-10, 10-15, and 15-20 cm bins all increase away from the fault, while the proportion of 0-5 cm space drops from 50-60% in the first 4 m to under 40% towards the end of the pavement (Figure 8f). Note that spacing data was measured along fault parallel scanlines at 50 cm intervals, and is therefore only representative of changes in the along-strike spacing with distance.

[Figure 8 here]

4.2.2 Fracture distribution statistics

Along-strike variance (S^2) in fracture density (Figure 8g) decays more clearly and gradually with distance from the fault than observed in the transect studies (Figure 6c,d). The Semi-Interquartile Range (SIR), that excludes outliers, shows a similar inverse relationship with distance (Figure 8h), suggesting that the observed spread of fracture densities in Figure 8a is not caused by outlying measurements. Both S^2 and SIR show a reversal of the inverse relationship in the 1 m closest to the fault core, with a sharp inflection at around 1.5 m (Figure 8g,h). This is likely caused by partial pulverisation, which effects the fracture density measurements in that zone. When the values at 0.5 and 1 m are removed, the data exhibits a linear and exponential inverse relationship with distance for SIR and S^2 respectively.

Both the minimum and maximum fracture densities decrease with distance from the fault and display concave up decay profiles, but with a steeper decay rate for the maximum density curve (Figure 8j). This suggests that distance has a stronger effect on the maximum fracture density than the minimum, which results in a decrease in the difference between the maximum and minimum with distance from the fault.

4.2.3 2D analysis of meso-scale fractures

The digitised 2D fracture network was analysed using the ‘Estimated Intensity, P21’ function in FracPaQ, which produced a contour map of fracture intensity on the pavement (Figure 9). Fracture intensity is defined as fracture length per area. The function is performed for each pixel of the fracture network, with the calculation considering a radial area based on the size of the scan circle (sampling area) defined in the FracPaQ GUI.

[Figure 9 here]

Absolute values of intensity depend on the calculation area; thus, the relative distribution of the fracture intensity can only be evaluated on the measurement scale defined by the scan circle. Image and tracing resolution limit the smallest scan circles to 5 cm diameter, while outcrop size limits diameters to several metres. We performed multiple iterations using scan circles ranging between 0.1-1.3 m diameter to assess the impact of scale on fracture intensity results. Larger diameters smoothed the distribution, reducing the contrast between nearby peaks and troughs, while small diameters amplify the heterogeneity. We identified three groups of scan circles that depict distinctly different fracture intensity patterns over two discrete scales. Between 0.24-0.55 m diameter, the outputs all show the same clear decimetre scale distribution (Figure 9c). This distribution changes with scan circle size until >0.8 m after which most of the decimetre scale features vanish and larger metre scale patterns emerge (Figure 9d). Below 0.24 m the results become more variable between iterations. We choose scan circles of 0.38 m and 1.14 m diameter as representative of the dm and m-scale distributions respectively (Figure 9c,d).

At both the dm and m-scale, damage accumulates into high and low intensity clusters, that form a patchy distribution with a weakening trend away from the fault. On the scales analysed, no part of the outcrop exhibits zero intensity which indicates fracture spacing of <10 cm between all sets. There is some apparent alignment of nodes and anti-nodes into weak 'corridors' at a high angle to the main fault trace. These are secondary features to the main quasi-cellular patterns that appear discreetly at both the dm and m-scale.

The wedge-shaped distribution of fracture density measurements with fault perpendicular distance observed in both the 1D pavement analyses (Figure 8a) and the wider transect study (Figure 6a,b) can also be interpreted from the fracture intensity map (Figure 9d), where the absolute difference between peaks and troughs (hot and cold colours) becomes smaller with distance from the fault. Peaks change from 50 to 26 m^{-1}, while troughs change from 24 to 10 m^{-1} over the length of the pavement. The greatest relative difference between node and anti-node intensities is marginally larger closer to the fault with up to 400% variation in the first 4 m compared to 300% after 14 m. This indicates that although absolute spread increases towards the fault, there appears to be a fairly consistent relative spread between 0-17 m.

4.2.4 Minor subsidiary fault distribution

Based on visual interpretation of Figures 9c-e, there is generally a good agreement between the locations of minor subsidiary faults and increased damage intensity. Specifically, high-intensity patches in the dm-scale distribution correlate well with where subsidiary faults interact or terminate (Figure 9c). Low-intensity patches are primarily located within the blocks bound by minor subsidiary faults, as well as along portions of their length where there is no interaction with other subsidiary faults. The metre-scale distribution shows a slightly more tenuous link, although generally speaking, higher intensities are found where more subsidiary faults interact (Figure 9d).

If meso-damage heterogeneity is controlled by minor subsidiary faults in the damage zone, we would expect to see more minor subsidiary faults where we observe the largest meso-fracture heterogeneity. We therefore completed a FracPaQ analysis on the digitised subsidiary fault map (Figure 9e), and find that fault intensity increases towards the fault core where heterogeneity is also highest. We also see that the amount of tips and intersections between minor subsidiary faults decreases with distance from the fault core.

5 Discussion

In this study we have presented a comprehensive high-resolution dataset quantifying the amount and distribution of fracture damage surrounding the seismically active Borrego Fault. We used a variety of sampling methodologies and analyses to assess the overall structure of the Borrego Fault, observing patterns in fracture heterogeneity in the damage zone that display systematic spatial relationships to minor subsidiary faults and distance from the main Borrego Fault. Such insights allow us to interpret mechanisms for the formation of this heterogeneity in the damage zone, and contribute improvements to existing fault damage zone evolution models.

5.1 *Structure of the Borrego Fault*

There are several important characteristics that differentiate the fault structure of the NW and SE Borrego Fault segments: Orientation, core structure, displacement magnitude, slip vector, and macro-damage complexity. These differences are so considerable that we suggest that for the purpose of comparison they can be treated as two separate faults. By doing so, observations of systematic trends in heterogeneity along both segments can reasonably indicate that this feature might also be observed along other faults.

5.1.1 Estimation of damage zone width

The average fracture density for the NW and SE fault segments both exhibit a concave up distribution with distance from the fault core (Figure 6a,b), which is similar to damage profiles observed on many other faults worldwide (e.g. Mitchell and Faulkner, 2009; O'Hara et al., 2017; Savage and Brodsky, 2011). Fracture density with distance from the fault core follows a power law distribution for both fault segments. We established a damage zone width on the footwall section of the fault, of 82 m [51-170 m] for the NW segment, and 122 m [37-519 m] for the SE segment. Fracture density results from the pavement yield a DZW of 90 m [44-258 m], which is consistent with the NW transects. Compared with studies on the relationship between damage zone width-displacement (Briere, 2000; Choi et al., 2016; Evans, 1990; Faulkner et al., 2011; Savage and Brodsky, 2011), these results are within error of the expected range of 30-1000 m for total fault zone width (Savage and Brodsky, 2011), and 20-140 m for footwall DZW in fractured rock (Choi et al., 2016). It remains unclear whether deviation in the DZWs of individual transects from the average DZW is related to undulation in the DZW over hundreds of metres along-strike, or simply due to inherent methodology errors/bias. For the pavement, any deviation in DZW is a true error as the transect spacing is too small to expect DZWs to vary by up to 110m (~200%). Note that the long tail of a power law distribution means that error in background densities yields very large changes to the DZW.

5.1.2 Damage heterogeneity

We observe an increasing spread of the data towards the fault, forming a distinctive wedge-shaped distribution in the scatter plots (Figure 6a,b and Figure 8a). We use the variance of this data as a direct proxy for fracture heterogeneity. The improved coverage of the 2D study allowed a more thorough investigation of the variance trends that we initially observed in the transect study. The abrupt 13-15 m transition in variance initially observed in the transect study was not observed in 2D, and we instead noted a more gradual variance increase from approximately 16 m towards the core. The statistical measures of the spread of the data from the pavement (Figure 8g,h) show inverse exponential (S^2) or quasi-linear (SIR) relationships with distance that intersect the x-axis between 18-20 m, but reach the background levels slightly closer to the fault core. This suggests that the outer section (>18 m) of the damage zone has a relatively constant background level variance in fracture density that increases at an exponential rate between 18-16 m from the fault. The abrupt variance transition identified from transect data (Figure 6c,d) is likely the result of incomplete sampling. We can thus define an inner and outer damage zone, where the inner damage zone is characterized by increased heterogeneity. This wedge shaped distribution can also be seen in historical datasets (e.g. Micarelli et al., 2006a; O'Hara et al., 2017; Schulz and Evans, 2000; Smith et al., 2013), although as far as the authors are aware, has never been addressed in discussions. Schulz and Evans (2000) go as far as drawing a wedge-shaped envelope around their data points (representing a minimum and maximum damage range), but make no comment on the widening trend towards the fault.

The observed variance profile can be explained by a local, quasi-cellular damage distribution visible in the fracture intensity maps (Figure 9). This decimetre and metre-scale patchiness likely causes much of the scatter observed in datasets of previous transect studies (at least in crystalline rock) that has previously been attributed to a “natural” or “background” random heterogeneity (Caine et al., 2010; Gudmundsson et al., 2002; Gudmundsson et al., 2010). The results in this study, however, show that there is a clear trend in variance with distance from the fault, which links to a systematic increase in meso-damage heterogeneity close to the fault. In statistics, this systematic trend in variance is called heteroscedasticity, and appears to be an inherent property of the meso-damage generating process. A description of the implications of this on choosing applicable model estimators is included in SI 3.6.

5.2 *Evolution of damage zone heterogeneity*

Our data shows a clear increase in heterogeneity of fracture density with increasing proximity to the fault core, which is likely due to the presence of localised damage surrounding subsidiary fault structures. We now consider the following: (1) how damage is localised to form the heterogeneous, patchy network; and (2) how the variance of fracture density is amplified within that pattern of distribution, particularly as we approach the fault.

5.2.1 Role of minor subsidiary faults

Our work shows a strong correlation between mesoscopic fracture intensity and minor shear fractures in the damage zone (Figure 9c), and both of these structural elements increase in intensity toward the fault core. This demonstrates a strong strain gradient within the damage zone. When combined with the intensity gradient, the gradual rotation of minor subsidiary faults towards the core (Figure 7d, Figure 9) indicates that they formed under the influence of a stress field modified by the Borrego Fault, which hence also suggests that they postdate the formation of the Borrego Fault. Additionally, lack of increased alteration along many minor subsidiary faults on the pavement indicate that these faults formed at lower P-T conditions and/or reduced fluid-rock ratios (Lawther et al., 2016). While we argue that this evidence suggests many subsidiary faults formed at mature stages of the Borrego Fault, we cannot rule out the possibility that some faults formed early in the evolution of the Borrego Fault. Relationships between mesoscopic fracture and minor subsidiary faults in the damage zone present a classic conundrum of which came first, “the chicken or the egg?” There is general consensus that small faults evolve into larger faults through the formation of mechanical linkages, stress concentration at fracture tips, and strain softening associated with progressive cataclasis (e.g. Cowie and Scholz, 1992; Dawers and Anders, 1995; Segall and Pollard, 1983). Therefore, it is likely that pre-existing weaknesses produce heterogeneities in mesoscopic fracture intensity, which in turn leads to further localization of strain and formation of subsidiary faults at larger scales.

The spatial distribution of subsidiary faults and damage heterogeneity over smaller scales may be used to constrain their relative formation ages. Importantly, the distribution of decimetre scale high intensity patches (nodes) observed on the pavement appears to be strongly associated with zones of interaction between minor subsidiary faults, and the tip zones of individual minor subsidiary faults (Figure 9c). We hypothesise that this is predominantly due to the increased complexity and intensity of the 'macro-damage' (as we defined in the introduction) distributed around the subsidiary faults in those zones (e.g. Kim et al., 2004). In this case macro-damage forming around these subsidiary faults is part of the meso-damage when considered relative to the Borrego Fault. Consequently, we suggest that much of the observed patchiness, at least at the decimetre scale, was produced as a result of stress concentration during the formation and growth of minor subsidiary faults in the damage zone. This may indicate pseudo-fractal scaling of processes in the damage zone, whereby heterogeneity in the distribution of meso-scale damage along the main fault, is controlled by the distribution of macro-scale fractures along subsidiary faults. The data demonstrates the importance of minor subsidiary faults in producing damage in the damage zones of large seismogenic faults. This is consistent with the 'slip-patch' model of damage zone growth proposed by Shipton and Cowie (2003), and supports the hypothesis that incremental slip events contribute to the progressive development of the mesoscopic fracture fabric of a fault zone (Savage and Brodsky, 2011).

Increased intensity of minor subsidiary faults towards the core leads to more interaction between faults and therefore more high intensity patches (Figure 9). Two things are necessary to progressively increase variance by increasing the number of nodes: First, the blocks between subsidiary fractures should remain relatively undeformed, and second, the number of interaction and tip zones, and therefore the number of high intensity patches, should increase. Once areas of high fracture intensity are developed, the resultant reduction in elastic moduli (e.g. Bruhn et al., 1994; Faulkner et al., 2006; Griffith et al., 2012) preferentially focuses further fracturing in those patches. This helps to reduce stress concentration in neighbouring intact blocks, limiting their internal deformation and exacerbating the systems variance over time. Intact blocks are likely to reduce in size over time by progressive growth of new minor subsidiary faults and by damage migrating incrementally inwards from the edges. The heterogeneity remains observable however as long as the blocks remain larger than the sampling scale. As strain accumulates, the intact blocks likely shrink to the point that they cease to exist at a given scale. Such a transition could be associated with the transformation of rock volumes of the inner damage zone to form new material that is added to the fault core.

Fracture intensity and subsidiary structures have been linked in several studies that noted increasing fracture intensity towards the fault cores of large subsidiary faults (e.g. Berg and Skar, 2005; Mayolle et al., 2019; Mitchell and Faulkner, 2009; Savage and Brodsky, 2011; Shipton and Cowie, 2001). Berg and Skar (2005) noted that many fractures were spatially associated with subsidiary faults, and suggested that subsidiary fractures often display increased intensity along their trace. Their examples consisted of faults with offsets of several metres and their own consistent, along strike, damage zones. Nevertheless, in their main outcrop fracture network, it appears that increased fracture intensity concentrates preferentially at the interaction and tips zones, and not along their entire length. A fracture intensity map would need to be made from their digitised fracture network in order to demonstrate this definitively. Shipton and Cowie (2003) provide a similar dataset and conclusions, but also include fracture intensity maps. Their results show higher damage intensities along the lengths of some of the large subsidiary faults, while smaller shear fractures (synonymous with their ‘slip-surfaces’ and our minor subsidiary faults) show a distinctly patchy fracture intensity along-strike, and clear peaks at the few interaction zones present in their outcrops. It is important to note that both of these datasets are obtained from porous sandstones with mesoscopic damage dominated by deformation bands that only accommodate a few millimetres of offset (Aydin and

Johnson, 1978; Shipton and Cowie, 2001). As faults are generally sparse in the damage zones of these examples, especially over the 10^0-10^1 m length scale, the effect of minor subsidiary structures contribute less to the generation of patchy heterogeneity.

5.2.2 Additional factors

Damage localisation in the observed patterns could also be explained by initial heterogeneities in the country rock properties, either in the lithologic/chemical composition of the granitoid host rock, or pre-existing background damage (e.g. Brogi, 2011). However, our background fracture density analysis did not indicate significant pre-existing structural or chemical heterogeneities in the same patterns observed in the damage zone.

Major subsidiary faults with well-developed damage zones clearly have a significant influence on the larger scale (10’s of metres) distribution of damage in the damage zone. Corridors of high-density damage surrounding these larger faults, up to several metres wide, have been observed in multiple field studies (e.g. Mitchell and Faulkner, 2009; Schulz and Evans, 2000; Smith et al., 2013), and the tip and linking zones of these larger faults likely also produce zones of intensified damage at scales larger than those mapped here. While care was taken to remove these influences, we cannot rule out effects of larger subsurface or obscured structures on our dataset.

5.3 *Conceptual damage zone evolution model*

Our data suggests that fracture damage zones evolve primarily through the growth and nucleation of minor subsidiary faults, and the concentration of smaller fractures around their fault tips and interaction zones consistent with mechanisms suggested by Shipton and Cowie (2003) for the slip-patch model. As the fault matures, existing subsidiary faults grow and new, smaller shear fractures nucleate, preferentially in and towards the inner damage zone (Gudmundsson et al., 2010) where reduced strength and elastic moduli favour fracturing. This creates a positive feedback where, with more fault tip and interaction zones, more high fracture intensity patches are generated, increasing the variance towards the fault core over time (Figure 10).

Variance (including S, and SIR) can be increased through one of two processes, (1) by increasing the total difference between the minimum and maximum densities, or (2) by changing the distribution of densities within the spread so that there is a higher proportion of measurements at both extremes (i.e. a shift from normal to bimodal distribution). The minimum meso-fracture density cannot decrease over the lifetime of a fault (at shallow P-T conditions, with low fracture healing rates), and maximum fracture densities are similar along both mature and immature faults (i.e. 10^1-10^3 m displacements) (Mitchell and Faulkner, 2009). Therefore, the spread of fracture densities does not increase once the damage maximum is formed, and probably changes very little with increasing fault maturity. This suggests that variance can only increase over time by shifting the fracture density distribution at a given distance towards a more bimodal distribution. This is achieved by increasing the number of fracture density peaks while maintaining a relatively constant minimum density.

Using a space-for-time substitution we interpolate that minor subsidiary fault density increases close to the main fault as it matures, resulting in more tip and interaction zones. This results in an increase of high-intensity damage patches, while the blocks between minor subsidiary faults remain comparatively undeformed, conserving the lower minimum fracture intensity. We thus expect a rise in the variance in the damage zone close to the fault core, that decays exponentially to background variance at a shorter distance than the average fracture density decays to the background fracture density. We show that the damage zone is divided into an inner and an outer zone based on increased complexity caused by minor subsidiary faults, which is demonstrated by the increasing variance from background levels. In the case of the Borrego Fault this transition occurs at around 16 m from the fault core.

As low-damaged, inter-fault blocks get smaller through crosscutting by new minor subsidiary faults, the observed heterogeneity changes, transitioning towards smaller scales with increasing fault maturity. This is supported by the dm-scale pattern observed on the fracture intensity map (Figure 9c), where the low-intensity patches, close to the fault, are smaller and account for less area than the high-intensity patches, whereas the opposite is observed further from the fault. The apparent shift indicates that as the fault grows, the distribution of damage transforms from large troughs with small, infrequent peaks, to small troughs separated by larger, linked peaks (Figure 10).

[Figure 10 here]

5.4 *Assessment of methodologies for fracture density quantification: 1D vs 2D*

We note marked improvement in the observation of the fault zone structure with increased sampling resolution and density, particularly in relation to heterogeneity in the damage zone. From our dataset we can compare 4 different resolution scales: (1) single transect studies with point measurements perpendicular to a fault; (2) diffuse multi-transect studies over several hundred metres along-strike; (3) concentrated multi-transect studies performed on a single outcrop with near-continuous data coverage; and (4) high-resolution 2D mapping of fractured outcrops.

1D transects show significant deviation, up to 50%, in DZW from the average damage zone trend, for both the widely spaced transects (with an average of three measurements at each sampling interval), and for densely spaced transects on the same outcrop (pavement transects). We therefore conclude that measurements from single transects do not fully represent the fault damage zone, even when three measurements are taken at each sampling interval. The common practice technique of averaging two or more transects provides a more representative damage zone profile, but conceals the fundamental property of variance in fracture density. However, uncertainty remains regarding how much variation in transect DZWs are a product of measurement error or method uncertainty, rather than real changes in the DZW along-strike. The concentrated multi-transect study on the pavement demonstrates that relative percentage differences of 88% can be explained by incomplete sampling of the heterogeneous damage profile for transects that did not extend through the damage zone. Exponential and logarithmic decay models have shorter tails which reduces the deviation between individual transects by a factor of ~10 (see SI 3.4). Whatever the cause, our data shows significant errors related to deriving the representative DZW, and even when an average representative transect is produced, these errors should be provided to account for any uncertainty.

While the high-resolution digital fracture network undoubtedly allows for more detailed and varied analysis, the necessary outcrop quality and additional time costs of manually tracing fractures makes it impractical in most fault studies. A 3D plot of fracture densities from the 9 continuous box-count transects (Figure 11) shows that several of the key observations from the 2D analysis (section 4.2.3) do not necessitate digitising the fracture network. For example, a metre to sub-metre heterogeneity pattern can be discerned from the 3D plot, which is similar to the fracture intensity map generated in FracPaQ. While the resolution of the plot derived from the continuous box-count transects is certainly lower than the fracture intensity map (50-100 cm rather than 10-30 cm), many of the same high and low intensity patches were observed (marked in Figure 11).

We show that the spreading trend can be identified from 4 transects, each with 2-3 discrete measurements at every interval (Figure 6). From continuous along-strike sampling with at least 9 measurements we can build a more complete picture of the heterogeneity, and quantify the system's variance trend (Figure 9). Based on the comparison of results from the different methodologies, we suggest that the best way to sample outcrop-scale heterogeneity, when either time or access to good 2D outcrops is limited, is to increase the number of non-overlapping measurements at each transect, rather than increasing the number of transects.

[Figure 11 here]

Sample scale also plays an important role in observing damage heterogeneity. Measurements at scales larger than the density heterogeneity scale average the difference between high- and low-density patches. Along the Borrego Fault we sampled the transects using a 30 cm measurement window, so we were more likely to collect a representative coverage of the dm-scale meso-damage pattern (Figure 9c). Sampling with a 1 m measurement window might have suppressed the difference sufficiently to conceal the variance trends observed in the multi-transect study. We hypothesise that the scale of heterogeneity might evolve over the lifetime of a fault, progressing towards smaller scales as intact blocks are gradually consumed by minor subsidiary faults. Thus, a changing scale of heterogeneity should be considered when choosing the sampling scale for a given fault study, specifically on more mature faults.

Clearly, more measurements (higher sampling density) allows us to more accurately observe the details of fracture distribution, but it also requires proportionally more time to collect these measurements. While high-resolution 2D fracture maps provide useful insights into damage distribution, they are also unnecessary for simply determining the DZW of a fault. For future meso-scale damage zone studies, we suggest the following 'best practice' methods to capture as much of the damage characteristics as possible, and to obtain a more representative damage zone profile:

1. For simple damage zone width studies:
    - i. Measure multiple transects at various distances along-strike to account for a potentially undulating damage zone width. Check that fault displacement is consistent at all of these transects, and hence does not influence the DZW.
    - ii. Take at least two measurements at every sampling location on each transect, giving a minimum and maximum damage value. Ideally a third measurement for the 'representative' damage at each distance from the fault should also be collected.
    - iii. Ensure shorter sampling intervals in the inner damage zone where the greatest rate of damage decay occurs.
2. For more detailed datasets:
    - i. Where good quality outcrops exist, perform at least one concentrated multi-transect study to quantify metre to sub-metre scale heterogeneity and to verify the existence of systematic change in variance (heteroscedasticity) in the dataset. For this, a high-

resolution digital fracture network is unnecessary, as it requires a significant time cost. Similar results can be obtained by collecting near continuous point measurements of fracture intensity using line counting methods.

ii. Measurement lengths should be dependent on the smallest fracture spacing, but are ideally in the 30-50 cm range to best capture sub-metre heterogeneity.

iii. Mapping of both minor and major subsidiary faults is crucial to compare with any spatial trends in fracture density.

5.5 *Implications*

Our results demonstrate a clear heterogeneity in both the amount and the distribution of fracture damage adjacent to the fault core. This heterogeneity decreases to background levels over a distance shorter than the measured damage zone width. Fracture damage provides a first order control on fluid flow in tight rocks, so that mineralisation that occurs due to the circulation of fluids in the damage zone will be governed by the distribution of this heterogeneity. Therefore, we infer that permeability in the damage zone is focused into patches of high-density fracture damage along the zones of interaction between minor subsidiary faults. These quasi-cellular regions of high permeability in two dimensions are likely to form a well-connected network in three dimensions, with sub-vertical conduits governed by the dominant minor subsidiary fault orientation acting as the principal fluid pathway in the damage zone.

Many studies now use realistic damage profiles as inputs for rupture propagation models (e.g. Cappa, 2011; Okubo et al., 2019; Thomas and Bhat, 2018). We suggest that such heterogeneity should be incorporated both along strike and with distance from the fault. Additionally, models of the coseismic evolution of faults should consider that damage heterogeneity increases with subsequent ruptures. Depending on the scale of earthquake propagation, these heterogeneities may influence wave propagation and affect dynamic processes such as thermal pressurisation and pulverization.

6 Conclusions

We demonstrate that mm-cm resolution fracture mapping provides a more accurate representation of the distribution of damage at meso-scales relative to off-fault damage characterised from 1D datasets. This allows for improved quantitative analysis of the damage zone and gives better insights into the mechanisms that control fault evolution.

Our key observations are that variance (i.e. a spatial spreading of fracture densities) in damage increases with proximity to a fault, and that seismically active faults in crystalline rocks display a patchy distribution of fracture damage with discreet patterns over decimetre and metre scales. The observed variance trend is the result of both the ratio and disparity between high- and low-intensity patches in the decimetre-scale distribution increasing towards the fault core. We suggest that the pattern is controlled by the distribution of macro-damage produced on shear-accommodating minor subsidiary fractures, with most patches of high fracture intensity corresponding to areas of complexity at the tip and interaction damage zones of these fractures. This demonstrates the importance of minor subsidiary faults in the evolution of off-fault damage, and is consistent with existing models of fault zone growth, such as the modified slip-patch model (Shipton and Cowie, 2003). Thus, apparent outcrop-scale disorganised heterogeneity is more systematic than first assumed. We used these systematic trends to identify an inner and outer damage zone that can be separated based on where the variance begins to increase above the background noise. From these results we presented a conceptual model for damage zone evolution in which minor subsidiary faults continue to nucleate and grow throughout the development of the fault, leading to increased damage heterogeneity with fault maturity.

Where detailed mapping is not feasible (e.g. limited exposure or time constraints), the increase in variance can be observed, albeit with reduced accuracy, using high-density sampling of fracture density along multiple transects. Four transects appear to be sufficient, but more importantly, multiple measurements, at each distance along a transect, will better uncover smaller scale heterogeneities.

Our data indicates that fault rupture propagation models should consider heterogeneous regions of damage distribution, not only along the strike of a fault, but also trends in damage heterogeneity in the rock perpendicular to a fault.

7 Acknowledgements

Funding was provided by NERC grant NE/M004716/1 to TMM and an RTSG to GAO from the London NERC DTP. Fieldwork was made possible by the generosity of colleagues at both SDSU and CICESE. Thanks goes to Taylor Hughes for providing essential support. We would also like to thank and acknowledge the contributions of S. Laubach and the three anonymous reviewers, whose insightful comments and suggestions have significantly improved the clarity and quality of this paper.

References:

Aben, F.M., Doan, M.-L., Gratier, J.-P., Renard, F., 2017. Coseismic damage generation and pulverization in fault zones: insights from dynamic Split-Hopkinson Pressure Bar experiments, in: Thomas, M.Y., Mitchell, T.M., Bhat, H.S. (Eds.), Fault Zone Dynamic Processes: Evolution of Fault Zone Properties During Seismic Rupture. John Wiley & Sons, pp. 47-80.

Aben, F.M., Doan, M.-L., Mitchell, T.M., Toussaint, R., Reuschlé, T., Fondriest, M., Gratier, J.-P., Renard, F., 2016. Dynamic fracturing by successive coseismic loadings leads to pulverization in active fault zones. Journal of Geophysical Research: Solid Earth 121, 2338-2360.

Andrews, D.J., 2005. Rupture dynamics with energy loss outside the slip zone. Journal of Geophysical Research: Solid Earth 110.

Aydin, A., Johnson, A.M., 1978. Development of faults as zones of deformation bands and as slip surfaces in sandstone. Pure and Applied Geophysics 116, 931-942.

Barnard, F.L., 1969. Structural geology of the Sierra de los Cucapas, northeastern Baja California, Mexico, and Imperial County, California.

Ben-Zion, Y., Ampuero, J.-P., 2009. Seismic radiation from regions sustaining material damage. Geophysical Journal International 178, 1351-1356.

Ben-Zion, Y., Sammis, C.G., 2003. Characterization of fault zones. Pure and Applied Geophysics 160, 677-715.

Berg, S.S., Skar, T., 2005. Controls on damage zone asymmetry of a normal fault zone: outcrop analyses of a segment of the Moab fault, SE Utah. J Struct Geol 27, 1803-1822.

Bistacchi, A., Massironi, M., Menegon, L., 2010. Three-dimensional characterization of a crustal-scale fault zone: The Pusteria and Sprechenstein fault system (Eastern Alps). J Struct Geol 32, 2022-2041.

Brantut, N., Mitchell, T.M., 2018. Assessing the Efficiency of Thermal Pressurization Using Natural Pseudotachylyte□Bearing Rocks. Geophys Res Lett 45, 9533-9541.

Briere, P.R., 2000. Playa, playa lake, sabkha: Proposed definitions for old terms. Journal of Arid Environments 45, 1-7.

Brogi, A., 2008. Fault zone architecture and permeability features in siliceous sedimentary rocks: Insights from the Rapolano geothermal area (Northern Apennines, Italy). J Struct Geol 30, 237-256.

Brogi, A., 2011. Variation in fracture patterns in damage zones related to strike-slip faults interfering with pre-existing fractures in sandstone (Calcione area, southern Tuscany, Italy). J Struct Geol 33, 644-661.

Bruhn, R.L., Parry, W.T., Yonkee, W.A., Thompson, T., 1994. Fracturing and hydrothermal alteration in normal fault zones. Pure and applied geophysics 142, 609-644.

Caine, J.S., Bruhn, R.L., Forster, C.B., 2010. Internal structure, fault rocks, and inferences regarding deformation, fluid flow, and mineralization in the seismogenic Stillwater normal fault, Dixie Valley, Nevada. J Struct Geol 32, 1576-1589.

Callahan, O.A., Eichhubl, P., Olson, J.E., Davatzes, N.C., 2019. Fracture Mechanical Properties of Damaged and Hydrothermally Altered Rocks, Dixie Valley□Stillwater Fault Zone, Nevada, USA. Journal of Geophysical Research: Solid Earth 124, 4069-4090.

Cappa, F., 2011. Influence of hydromechanical heterogeneities of fault zones on earthquake ruptures. Geophysical Journal International 185, 1049-1058.

Cappa, F., Perrin, C., Manighetti, I., Delor, E., 2014. Off-fault long-term damage: A condition to account for generic, triangular earthquake slip profiles. Geochemistry, Geophysics, Geosystems 15, 1476-1493.

Chester, F.M., Chester, J.S., 2000. Stress and deformation along wavy frictional faults. Journal of Geophysical Research-Solid Earth 105, 23421-23430.

Chester, F.M., Logan, J.M., 1986. Implications for Mechanical-Properties of Brittle Faults from Observations of the Punchbowl Fault Zone, California. Pure and Applied Geophysics 124, 79-106.

Chester, J.S., Chester, F.M., Kronenberg, A.K., 2005. Fracture surface energy of the Punchbowl fault, San Andreas system. Nature 437, 133-136.

Childs, C., Manzocchi, T., Walsh, J.J., Bonson, C.G., Nicol, A., Schöpfer, M.P.J., 2009. A geometric model of fault zone and fault rock thickness variations. J Struct Geol 31, 117-127.

Choi, J.-H., Edwards, P., Ko, K., Kim, Y.-S., 2016. Definition and classification of fault damage zones: A review and a new methodological approach. Earth-Science Reviews 152, 70-87.

Cowie, P.A., Scholz, C.H., 1992. Growth of faults by accumulation of seismic slip. J Geophys Res 97, 11,085-011,095.

Crider, J.G., Peacock, D.C., 2004. Initiation of brittle faults in the upper crust: a review of field observations. J Struct Geol 26, 691-707.

Dawers, N.H., Anders, M.H., 1995. Displacement-length scaling and fault linkage. J Struct Geol 17, 607-614.

Dor, O., Ben-Zion, Y., Rockwell, T.K., Brune, J., 2006. Pulverized rocks in the Mojave section of the San Andreas Fault Zone. Earth Planet Sc Lett 245, 642-654.

Dorsey, M.T., Rockwell, T.K., Girty, G.H., Ostermeijer, G.A., Browning, J., Mitchell, T.M., Fletcher, J.M., IN PREP. Evidence of Hydrothermal Brine Circulation Driving Elemental Mass Redistribution in an Active Fault Zone.

Dorsey, R.J., Umhoefer, P.J., 2012. Influence of sediment input and plate-motion obliquity on basin development along an active oblique-divergent plate boundary: Gulf of California and Salton Trough. Tectonics of Sedimentary Basins: Recent Advances, 209-225.

Dunham, E.M., Belanger, D., Cong, L., Kozdon, J.E., 2011. Earthquake Ruptures with Strongly Rate-Weakening Friction and Off-Fault Plasticity, Part 1: Planar Faults. Bulletin of the Seismological Society of America 101, 2296-2307.

Eichhubl, P., Davatz, N.C., Becker, S.P., 2009. Structural and diagenetic control of fluid migration and cementation along the Moab fault, Utah. AAPG Bulletin 93, 653-681.

Evans, J.P., 1990. Thickness-displacement relationships for fault zones. J Struct Geol 12, 1061-1065.

Evans, J.P., Forster, C.B., Goddard, J.V., 1997. Permeability of fault-related rocks, and implications for hydraulic structure of fault zones. J Struct Geol 19, 1393-1404.

Faulkner, D.R., Jackson, C.A.L., Lunn, R.J., Schlische, R.W., Shipton, Z.K., Wibberley, C.A.J., Withjack, M.O., 2010. A review of recent developments concerning the structure, mechanics and fluid flow properties of fault zones. J Struct Geol 32, 1557-1575.

Faulkner, D.R., Mitchell, T.M., Healy, D., Heap, M.J., 2006. Slip on 'weak' faults by the rotation of regional stress in the fracture damage zone. Nature 444, 922-925.

Faulkner, D.R., Mitchell, T.M., Jensen, E., Cembrano, J., 2011. Scaling of fault damage zones with displacement and the implications for fault growth processes. Journal of Geophysical Research: Solid Earth 116.

Fletcher, J.M., Teran, O.J., Rockwell, T.K., Oskin, M.E., Hadnut, K.W., Spelz, R.M., Lacan, P., Dorsey, M.T., Ostermeijer, G.A., Mitchell, T.M., Akciz, S.O., Hernandez-Flores, A.P., Hinojosa, A., Arregu-Ojeda, S., Peña-Villa, I., Lynch, D.K., 2020. An analysis of the factors that control fault zone architecture and the importance of fault orientation relative to regional stress. Geol Soc Am Bull.

Fletcher, J.M., Teran, O.J., Rockwell, T.K., Oskin, M.E., Hudnut, K.W., Mueller, K.J., Spelz, R.M., Akciz, S.O., Masana, E., Faneros, G., Fielding, E.J., Leprince, S., Morelan, A.E., Stock, J., Lynch, D.K., Elliott, A.J., Gold, P., Liu-Zeng, J., González-Ortega, A., Hinojosa-Corona, A., González-García, J., 2014. Assembly of a large earthquake from a complex fault system: Surface rupture kinematics of the 4 April 2010 El Mayor–Cucapah (Mexico) Mw 7.2 earthquake. Geosphere 10, 797-827.

Grasemann, B., Exner, U., Tschegg, C., 2011. Displacement–length scaling of brittle faults in ductile shear. J Struct Geol 33, 1650-1661.

Griffith, W.A., Mitchell, T.M., Renner, J., Di Toro, G., 2012. Coseismic damage and softening of fault rocks at seismogenic depths. Earth Planet Sc Lett 353, 219-230.

Griffith, W.A., Sanz, P.F., Pollard, D.D., 2009. Influence of Outcrop Scale Fractures on the Effective Stiffness of Fault Damage Zone Rocks. Pure and Applied Geophysics 166, 1595-1627.

Gudmundsson, A., Fjeldskaar, I., Brenner, S.L., 2002. Propagation pathways and fluid transport of hydrofractures in jointed and layered rocks in geothermal fields. J Volcanol Geoth Res 116, 257-278.

Gudmundsson, A., Simmenes, T.H., Larsen, B., Philipp, S.L., 2010. Effects of internal structure and local stresses on fracture propagation, deflection, and arrest in fault zones. J Struct Geol 32, 1643-1655.

Harris, R.A., Day, S.M., 1997. Effects of a low-velocity zone on a dynamic rupture. Bulletin of the Seismological Society of America 87, 1267-1280.

Healy, D., Rizzo, R.E., Cornwell, D.G., Farrell, N.J.C., Watkins, H., Timms, N.E., Gomez-Rivas, E., Smith, M., 2017. FracPaQ: A MATLAB™ toolbox for the quantification of fracture patterns. J Struct Geol 95, 1-16.

Hennings, P., Allwardt, P., Paul, P., Zahm, C., Reid, R., Alley, H., Kirschner, R., Lee, B., Hough, E., 2012. Relationship between fractures, fault zones, stress, and reservoir productivity in the Suban gas field, Sumatra, Indonesia. AAPG bulletin 96, 753-772.

Hernandez, A., Fletcher, J., Spelz, R., Rockwell, T., Teran, O., 2013. Paleoseismology of the imbricate fault array in the Sierra Cucapah, northern Baja California, Mexico, AGU Spring Meeting Abstracts.

Huang, Y., Ampuero, J.-P., Helmberger, D.V., 2014. Earthquake ruptures modulated by waves in damaged fault zones. Journal of Geophysical Research: Solid Earth 119, 3133-3154.

Huang, Y., Ampuero, J.P., 2011. Pulse□like ruptures induced by low□velocity fault zones. Journal of Geophysical Research: Solid Earth 116.

ISRM, 1978. Commission on Standardization of Laboratory and Field Tests: Suggested methods for the quantitative description of discontinuities in rock masses. International Journal of Rock Mechanics and Mining Sciences & Geomechanics Abstracts 15, 319-368.

Johri, M., Dunham, E.M., Zoback, M.D., Fang, Z., 2014a. Predicting fault damage zones by modeling dynamic rupture propagation and comparison with field observations. Journal of Geophysical Research: Solid Earth 119, 1251-1272.

Johri, M., Zoback, M.D., Hennings, P., 2014b. A scaling law to characterize fault-damage zones at reservoir depthsFault Damage Zones at Depth. AAPG Bulletin 98, 2057-2079.

Kim, Y.-S., Andrews, J.R., Sanderson, D.J., 2000. Damage zones around strike-slip fault systems and strike-slip fault evolution, Crackington Haven, southwest England. Geosciences Journal 4, 53-72.

Kim, Y.-S., Peacock, D., Sanderson, D.J., 2003. Mesoscale strike-slip faults and damage zones at Marsalforn, Gozo Island, Malta. J Struct Geol 25, 793-812.

Kim, Y.-S., Peacock, D.C.P., Sanderson, D.J., 2004. Fault damage zones. J Struct Geol 26, 503-517.

Kim, Y.-S., Sanderson, D.J., 2008. Earthquake and fault propagation, displacement and damage zones. Structural Geology: New Research 1, 99-117.

Knott, S.D., Beach, A., Brockbank, P.J., Lawson Brown, J., McCallum, J.E., Welbon, A.I., 1996. Spatial and mechanical controls on normal fault populations. J Struct Geol 18, 359-372.

Lawther, S.E., Dempster, T.J., Shipton, Z.K., Boyce, A.J., 2016. Effective crustal permeability controls fault evolution: An integrated structural, mineralogical and isotopic study in granitic gneiss, Monte Rosa, northern Italy. Tectonophysics 690, 160-173.

Lizarralde, D., Axen, G.J., Brown, H.E., Fletcher, J.M., González-Fernández, A., Harding, A.J., Holbrook, W.S., Kent, G.M., Paramo, P., Sutherland, F., Umhoefer, P.J., 2007. Variation in styles of rifting in the Gulf of California. Nature 448, 466-469.

Lockner, D., Naka, H., Tanaka, H., Ito, H., Ikeda, R., 2000. Permeability and strength of core samples from the Nojima fault of the 1995 Kobe earthquake, Proceedings of the international workshop on the Nojima fault core and borehole data analysis. Citeseer, pp. 147-152.

Love, A., 1927. A Treatise on the Theory Mathematical of Elasticity. Cambridge University Press, Cambridge, 643pp.

Loveless, S., Bense, V., Turner, J., 2011. Fault architecture and deformation processes within poorly lithified rift sediments, Central Greece. J Struct Geol 33, 1554-1568.

Madariaga, R., 1983. High frequency radiation from dynamic earthquake. Ann. Geophys. 1, 17-23.

Mayolle, S., Soliva, R., Caniven, Y., Wibberley, C., Ballas, G., Milesi, G., Dominguez, S., 2019. Scaling of fault damage zones in carbonate rocks. J Struct Geol 124, 35-50.

Micarelli, L., Benedicto, A., Wibberley, C.A.J., 2006a. Structural evolution and permeability of normal fault zones in highly porous carbonate rocks. J Struct Geol 28, 1214-1227.

Micarelli, L., Moretti, I., Jaubert, M., Moulouel, H., 2006b. Fracture analysis in the south-western Corinth rift (Greece) and implications on fault hydraulic behavior. Tectonophysics 426, 31-59.

Mitchell, T.M., Ben-Zion, Y., Shimamoto, T., 2011. Pulverized fault rocks and damage asymmetry along the Arima-Takatsuki Tectonic Line, Japan. Earth Planet Sc Lett 308, 284-297.

Mitchell, T.M., Faulkner, D.R., 2009. The nature and origin of off-fault damage surrounding strike-slip fault zones with a wide range of displacements: A field study from the Atacama fault system, northern Chile. J Struct Geol 31, 802-816.

Myers, R., Aydin, A., 2004. The evolution of faults formed by shearing across joint zones in sandstone. J Struct Geol 26, 947-966.

Noda, H., Lapusta, N., 2013. Stable creeping fault segments can become destructive as a result of dynamic weakening. Nature 493, 518-523.

O'Hara, A.P., Jacobi, R.D., Sheets, H.D., 2017. Predicting the width and average fracture frequency of damage zones using a partial least squares statistical analysis: Implications for fault zone development. J Struct Geol 98, 38-52.

Okubo, K., Bhat, H.S., Rougier, E., Marty, S., Schubnel, A., Lei, Z., Knight, E.E., Klinger, Y., 2019. Dynamics, radiation and overall energy budget of earthquake rupture with coseismic off-fault damage. arXiv preprint arXiv:1901.01771.

Peacock, D.C.P., Nixon, C.W., Rotevatn, A., Sanderson, D.J., Zuluaga, L.F., 2016. Glossary of fault and other fracture networks. J Struct Geol 92, 12-29.

Price, N.J., Cosgrove, J.W., 1990. Analysis of geological structures. Cambridge University Press.

Reches, Z., Dewers, T.A., 2005. Gouge formation by dynamic pulverization during earthquake rupture. Earth Planet Sc Lett 235, 361-374.

Rempe, M., Mitchell, T., Renner, J., Nippress, S., Ben-Zion, Y., Rockwell, T., 2013. Damage and seismic velocity structure of pulverized rocks near the San Andreas Fault. Journal of Geophysical Research: Solid Earth 118, 2813-2831.

Rempe, M., Mitchell, T.M., Renner, J., Smith, S.A.F., Bistacchi, A., Di Toro, G., 2018. The Relationship Between Microfracture Damage and the Physical Properties of Fault-Related Rocks: The Gole Larghe Fault Zone, Italian Southern Alps. Journal of Geophysical Research-Solid Earth 123, 7661-7687.

Rice, J.R., Sammis, C.G., Parsons, R., 2005. Off-fault secondary failure induced by a dynamic slip pulse. Bulletin of the Seismological Society of America 95, 109-134.

Rousseau, C.E., Rosakis, A.J., 2003. On the influence of fault bends on the growth of sub-Rayleigh and intersonic dynamic shear ruptures. Journal of Geophysical Research: Solid Earth 108.

Rowe, C.D., Moore, J.C., Remitti, F., Scientist, I.E.T., 2013. The thickness of subduction plate boundary faults from the seafloor into the seismogenic zone. Geology 41, 991-994.

Sagy, A., Korngreen, D., 2012. Dynamic branched fractures in pulverized rocks from a deep borehole. Geology 40, 799-802.

Savage, H.M., Brodsky, E.E., 2011. Collateral damage: Evolution with displacement of fracture distribution and secondary fault strands in fault damage zones. Journal of Geophysical Research: Solid Earth 116.

Scholz, C.H., 1987. Wear and Gouge Formation in Brittle Faulting. Geology 15, 493-495.

Schulz, S.E., Evans, J.P., 2000. Mesoscopic structure of the Punchbowl Fault, Southern California and the geologic and geophysical structure of active strike-slip faults. J Struct Geol 22, 913-930.

Segall, P., Pollard, D.D., 1983. Nucleation and growth of strike slip faults in granite. Journal of Geophysical Research: Solid Earth 88, 555-568.

Seront, B., Wong, T.-F., Caine, J.S., Forster, C.B., Bruhn, R.L., Fredrich, J., 1998. Laboratory characterization of hydromechanical properties of a seismogenic normal fault system. J Struct Geol 20, 865-881.

Shipton, Z.K., Cowie, P.A., 2001. Damage zone and slip-surface evolution over μm to km scales in high-porosity Navajo sandstone, Utah. J Struct Geol 23, 1825-1844.

Shipton, Z.K., Cowie, P.A., 2003. A conceptual model for the origin of fault damage zone structures in high-porosity sandstone. J Struct Geol 25, 333-344.

Sibson, R.H., 1986. Earthquakes And Rock Deformation In Crustal Fault Zones. Annu Rev Earth Pl Sc 14, 149-175.

Sibson, R.H., 1994. Crustal stress, faulting and fluid flow. Geological Society, London, Special Publications 78, 69-84.

Sibson, R.H., 2003. Thickness of the seismic slip zone. Bulletin of the Seismological Society of America 93, 1169-1178.

Smith, S.A.F., Bistacchi, A., Mitchell, T.M., Mittempergher, S., Di Toro, G., 2013. The structure of an exhumed intraplate seismogenic fault in crystalline basement. Tectonophysics 599, 29-44.

Teran, O.J., Fletcher, J.M., Oskin, M.E., Rockwell, T.K., Hudnut, K.W., Spelz, R.M., Akciz, S.O., Hernandez-Flores, A.P., Morelan, A.E., 2015. Geologic and structural controls on rupture zone fabric: A field-based study of the 2010 Mw 7.2 El Mayor–Cucapah earthquake surface rupture. Geosphere 11, 899-920.

Thomas, M.Y., Bhat, H.S., 2018. Dynamic evolution of off-fault medium during an earthquake: a micromechanics based model. Geophysical Journal International 214, 1267-1280.

Thomas, M.Y., Bhat, H.S., Klinger, Y., 2017. Effect of brittle off-fault damage on earthquake rupture dynamics. Fault zone dynamic processes: Evolution of fault properties during seismic rupture 227, 255-280.

Umhoefer, P.J., 2011. Why did the southern Gulf of California rupture so rapidly?—Oblique divergence across hot, weak lithosphere along a tectonically active margin. GSA Today 21, 4-10.

Walsh, J.B., 1965. The effect of cracks on the compressibility of rock. J Geophys Res 70, 381-389.

Wechsler, N., Allen, E.E., Rockwell, T.K., Girty, G., Chester, J.S., Ben-Zion, Y., 2011. Characterization of pulverized granitoids in a shallow core along the San Andreas Fault, Littlerock, CA. Geophysical Journal International 186, 401-417.

Williams, R.T., Goodwin, L.B., Mozley, P.S., 2017. Diagenetic controls on the evolution of fault-zone architecture and permeability structure: Implications for episodicity of fault-zone fluid transport in extensional basins. Geol Soc Am Bull 129, 464-478.

Wilson, J.E., Chester, J.S., Chester, F.M., 2003. Microfracture analysis of fault growth and wear processes, Punchbowl Fault, San Andreas system, California. J Struct Geol 25, 1855-1873.

Withjack, M.O., Jamison, W.R., 1986. Deformation produced by oblique rifting. Tectonophysics 126, 99-124.

Wu, C., Peng, Z., Ben-Zion, Y., 2009. Non-linearity and temporal changes of fault zone site response associated with strong ground motion. Geophysical Journal International 176, 265-278.

Xu, S., Ben-Zion, Y., Ampuero, J.-P., 2012. Properties of inelastic yielding zones generated by in-plane dynamic ruptures-II. Detailed parameter-space study. Geophysical Journal International 191, 1343-1360.

Table 1: Data and power law regressions from the eight individual transects, scatter plots, and averages for the NW and SE segments of the Borrego Fault

Transect ID	**Transect Length (m)**	**Damage Zone Width (DZW) (m)**	**Maximum Fracture Density (#m^{-1})**	**Distance of fracture density maxima from fault core (m)**	**R^2**	**Power Law Slope Coefficient (*n*)**
NW_T1	50	96.1 [67.9 - 162.8]	71	3.5[b]	0.93	0.304 [± 0.025]
NW_T2	65	72.3 [54.2 - 112.4]	74	8[b]	0.94	0.364 [± 0.028]
NW_T3	45	121.4 [81.6 - 222.5]	80	3.5	0.90	0.265 [± 0.025]
NW_T4	150	79.8 [54.0 - 144.7]	75	4	0.86	0.269 [± 0.032]
NW Scatter Plot		83.6 [51.3 - 181.8][a]			0.78	0.308 [± 0.015]
NW Average		81.9 [51.3 - 169.9][a]			0.96	0.314 [± 0.013]
SE_T1	150	99.1 [45.8 - 208.6]	73	2.5[b]	0.92	0.245 [± 0.019]
SE_T2	80	-	79	4.5	0.39	-
SE_T3[c]	3.5		81	0		
SE_T4	90	102.9 [47.8 - 215.3]	69	3.5[b]	0.98	0.247 [± 0.007]
SE Scatter Plot		111.9 [37.1 - 410.0][a]			0.64	0.216 [± 0.012]
SE Average		121.6 [36.9 - 518.5][a]			0.88	0.204 [± 0.014]

Results from exponential and logarithmic regression models can be found in Supplementary Information. All errors without symbols are derived using the uncertainty in background damage.
[a] *Combined error from 95% confidence interval (based on the standard error of the model) and uncertainty in average BFD*
- too much scatter to derive a reliable DZW (R^2 < 0.4)
[b] *Maxima is at the closest available measurement to the fault core (i.e. no measurement adjacent to FC).*
[c] *transects that are not long enough to individually derive an DZW*

Table 2: Data and power law regressions from each transect, spaced at 0.5 m along the river platform, the scatter plot of all this data, and the averaged transect.

Transect ID	**Damage Zone Width (DZW) (m)**	**Maximum Fracture Density (#m^{-1})**	**Distance of fracture density maxima from fault core (m)**	**R^2**	**Power Law Slope Coefficient (*n*)**
T2	97.2 [59.4 - 181.2]	412	1 - 1.5	0.58	0.421 [± 0.070]
T3	-	432	1 - 1.5	0.31	-
T4	133.9 [79.9 – 256.9]	512	1 - 1.5	0.52	0.403 [± 0.074]
T5	69.4 [45.9 – 116.7]	516	1.5 - 2	0.64	0.504 [± 0.073]
T6	51.5 [35.8 - 81.6]	452	2 - 2.5	0.80	0.571 [± 0.056]
T7	76.1 [49.4 - 131.4]	408	4.5 - 5	0.68	0.480 [± 0.061]
T8	69.4 [46.0 - 116.8]	464	1.5 - 2	0.68	0.504 [± 0.064]
Scatter Plot	*90.4 [45.6 - 241.0]*[a]			*0.60*	*0.445 [±0.024]*
Averaged	*89.9 [44.3 - 257.5]*[a]	*427*	*1 - 1.5*	*0.89*	*0.456 [±0.029]*

T1 and T9 only extend to half the outcrop (T1 from 0-8.25 m and T9 from 9.5-18.5 m), and as a result are not directly compared with T2-T8. The data on these two transects is still included in the scatter plot, graphs in Figure 8, and contributes to the average values. All errors without symbols are derived using only the uncertainty in background damage.

[a] *Combined error from 95% confidence interval (based on the standard error of the model) and uncertainty in average BFD.*

- too much scatter to derive a reliable DZW (R^2 < 0.4).

Damage Zone Heterogeneity on Seismogenic Faults in Crystalline Rock; a Field Study of the Borrego Fault, Baja California.

Figures

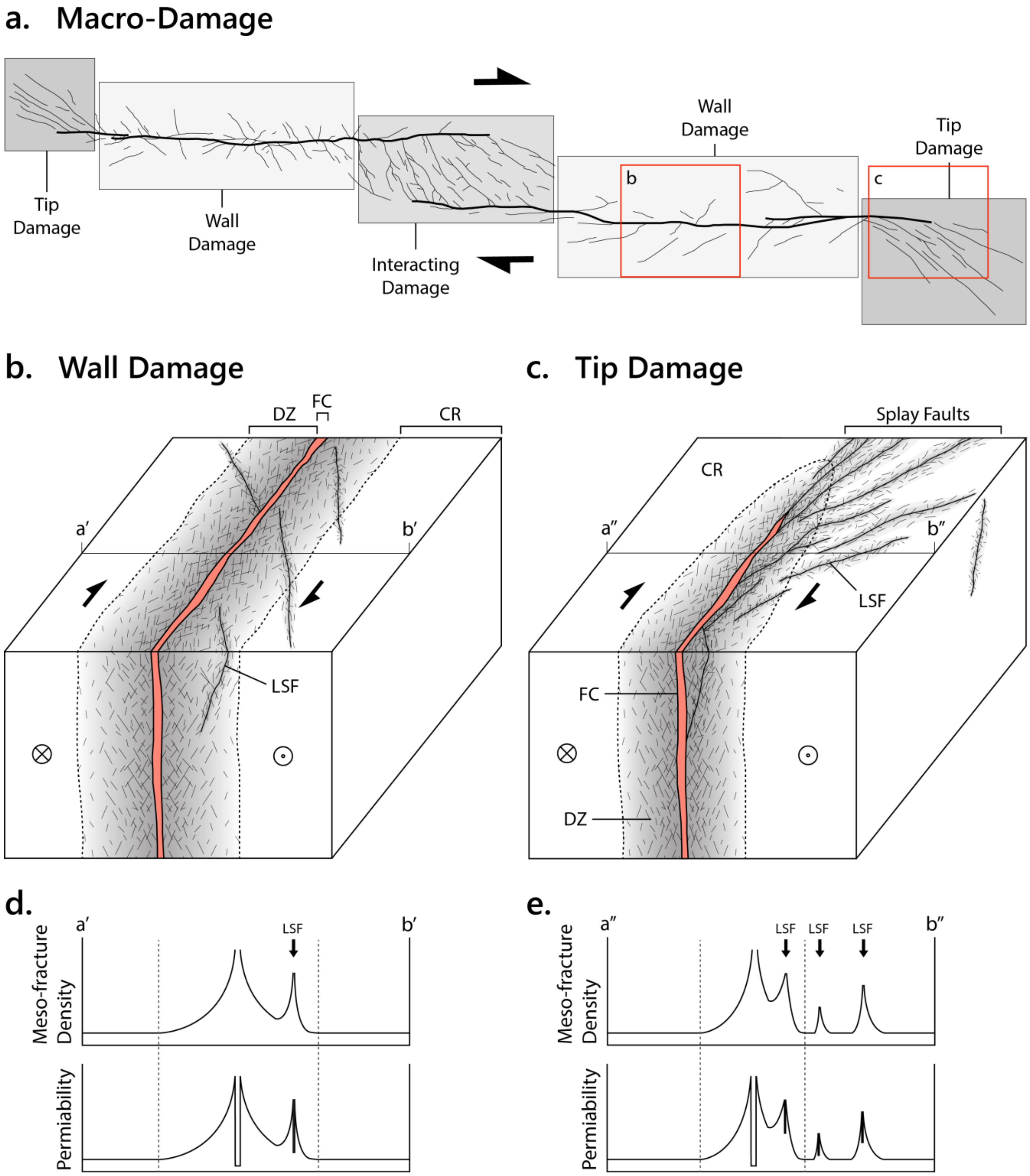

*Figure 1: Schematic representation of the distribution of damage around a fault collated and modified from various sources (Faulkner et al., 2003; Kim et al., 2004; Mitchell and Faulkner, 2009; Peacock et al., 2016; Shipton and Cowie, 2003). **a.** shows the distribution of macro-damage around a fault. The wider, more intensely damaged zones occur at the fault tips and areas of fault interaction. There is no scale on the image as this distribution is consistent along faults ranging all visible scales from cm-km. **b.** and **c.** show the distribution of meso-scale damage in a sheath around large faults, the width scaling with displacement so that it is widest near the centre (**b**), and tapers towards the tips (**c**). **d.** and **e.** The influence of large subsidiary faults that have their own macro- and meso-damage zone, is clearly shown in the simplified/averaged meso-fracture density and permeability transects (black arrows). CR – Country Rock; DZ – Damage Zone; FC – Fault Core; LSF – Large Subsidiary Faults.*

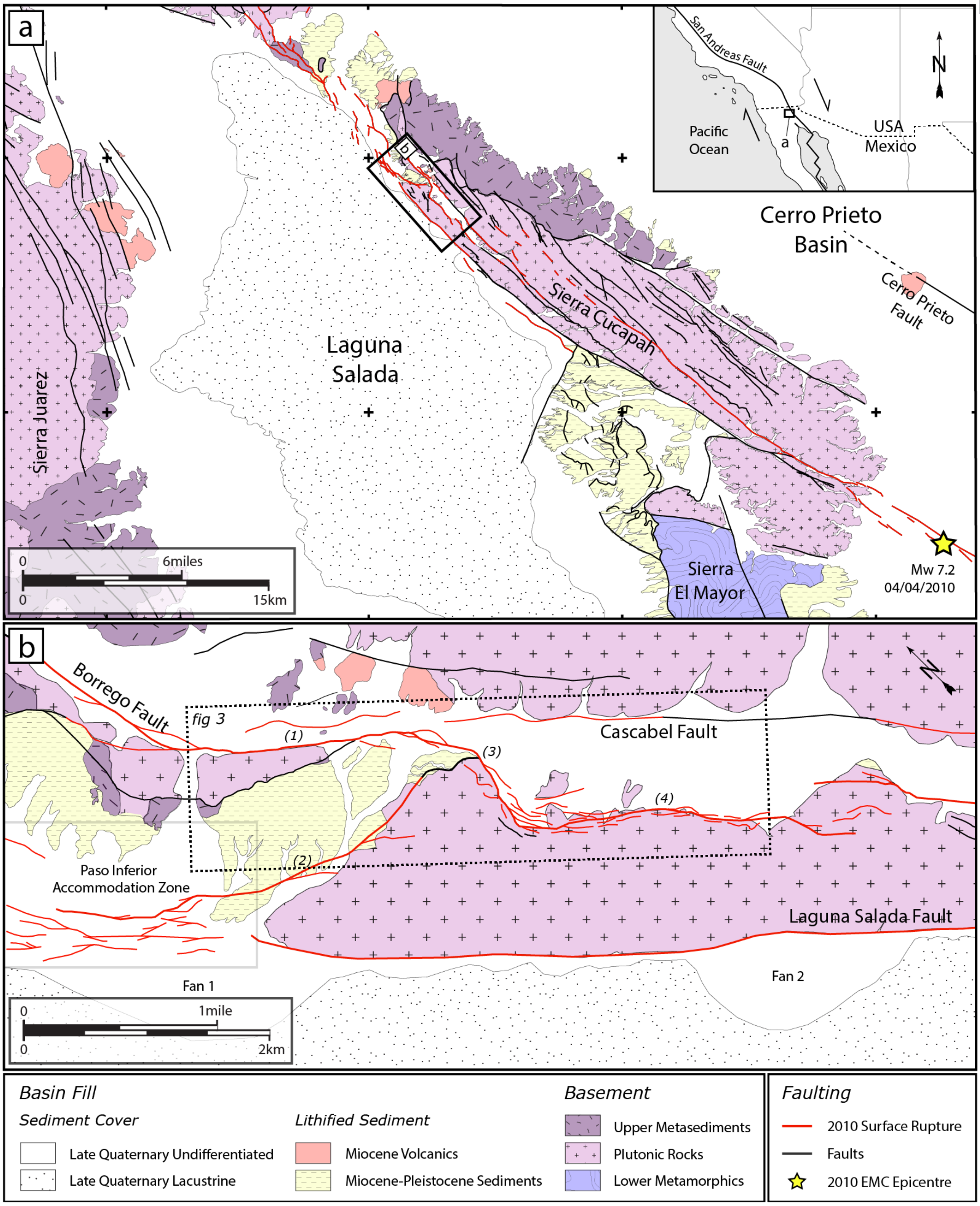

Figure 2: Regional and local geological map of the study area. ***a.*** *The metamorphic and plutonic basement of the Sierra Cucapah horst block bound to the SW and NE by the Laguna Salada and Cerro Prieto sedimentary basins. The yellow star indicates the epicentre of the Mw7.2 2010 El Mayor-Cucapah (EMC) earthquake which propagated NW along the path of the red fault lines (Fletcher et al., 2014).* ***b.*** *Local geology around the 5 km long section of the Borrego Fault studied in this paper. The fault consists of two distinct sections, NW and SE, separated by a 600 m northward bend and bifurcation at point (3). The SW section (4) dips gently towards the NE and has formed a wide array of fault scarps. The NW section has two segments, (1) a steep, linear strand continuous with the SW Borrego Fault, and (2) a gently dipping strand branching towards the west where it interacts with the buried Laguna Salada Fault to form the Paso Inferior accommodation zone. Both sections bound the narrow Borrego basin, forming an asymmetrical graben with the SW dipping Cascabel Fault. The two horst blocks, SW of (1) and (4), expose plutonic tonalite and granodiorite in which we performed detailed meso-fracture studies.*

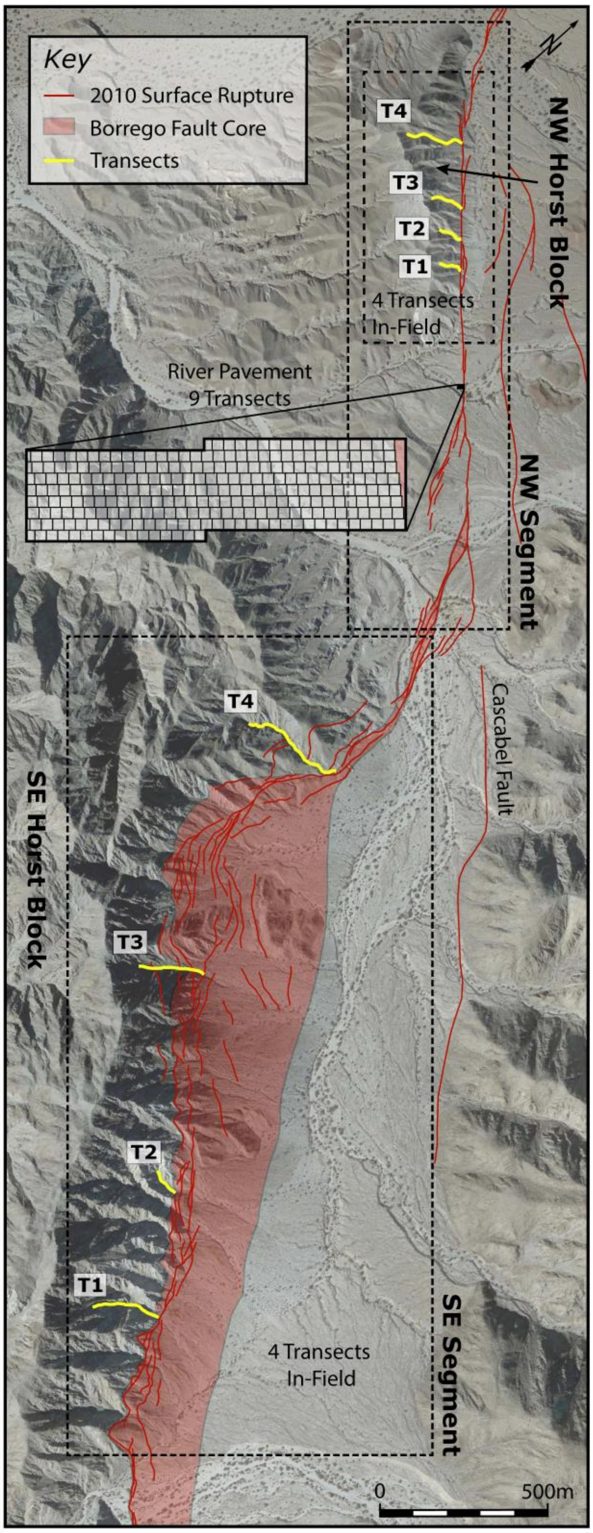

Figure 3: Locations of field sites along the Borrego Fault, split into NW and SE segments. In-situ measurements of meso-fracture density were collected along 8 transects in total, 4 along each segment. A detailed 2D fracture map was made from high resolution photographs on the river pavement which was then used to create nine transects for further analysis. On each segment the transects are numbered 1 to 4, starting from the Southeast (i.e. NW_T1 is the closest to the river pavement).

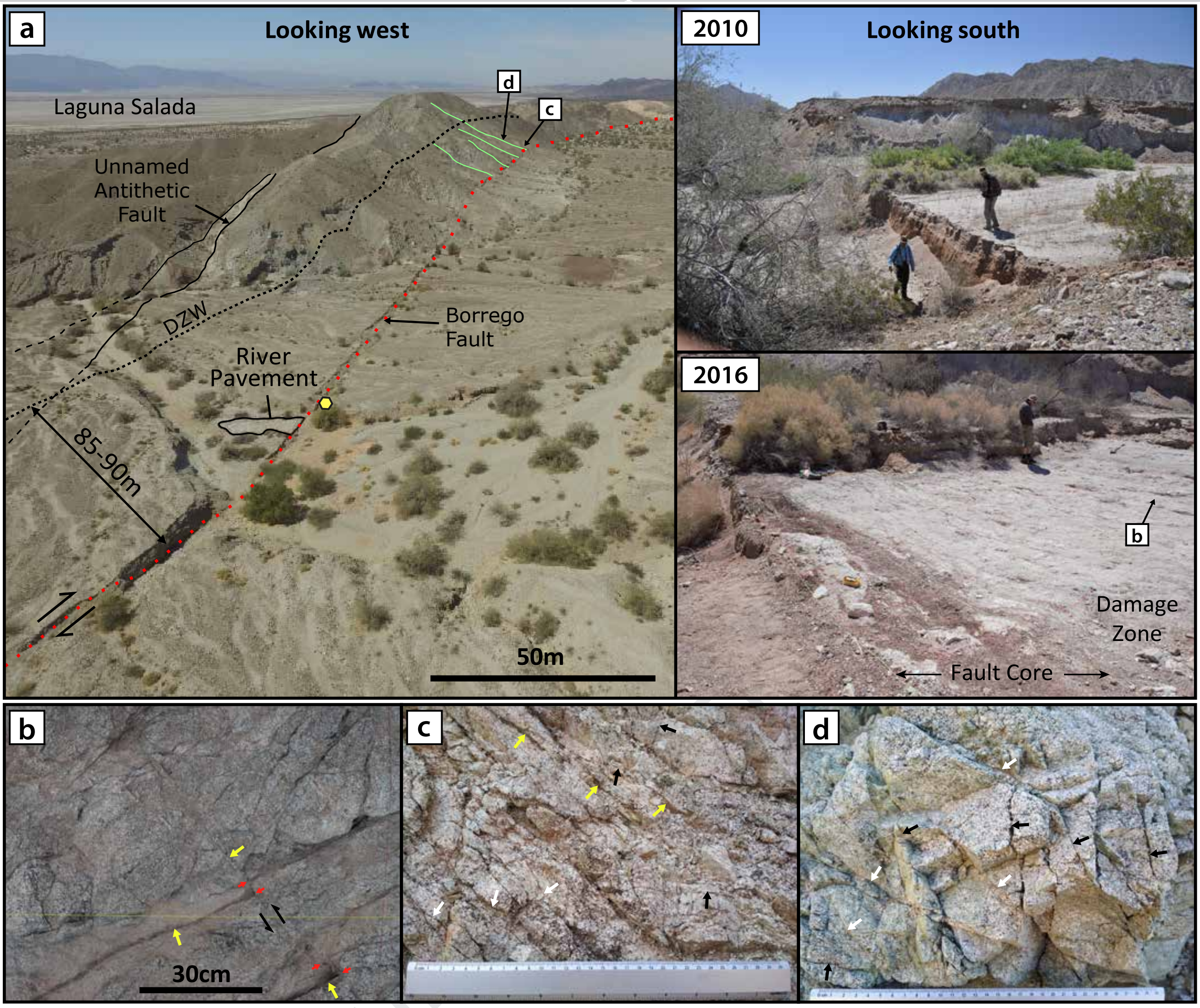

*Figure 4: **a.** Drone image of the NW horst-block with the Borrego Fault and unnamed antithetic fault illustrated for clarity. The red line indicates the 2010 EMC rupture surface along the Borrego and green lines show the locations of the 4 NW transects. The damage zone width (DZW) of 85-90 m, derived from transect and pavement studies (see results section), is marked by the dotted line and provides context for the 2D pavement study. The two images on the right show the Arroyo bed before (2010) and after (2016) flash floods that scoured off overlying sediments to expose the basement rocks. The photos were taken from the yellow dot, looking south towards the river outcrop. **b-d.** Field photos of meso-fractures from pavement and transects. Yellow arrows = minor subsidiary faults; White arrows = fractures with cataclasite infill; Black arrows = open fractures with no mineral infill. Several minor subsidiary faults on the pavement crosscut one another so that offsets may be measured (**b**).*

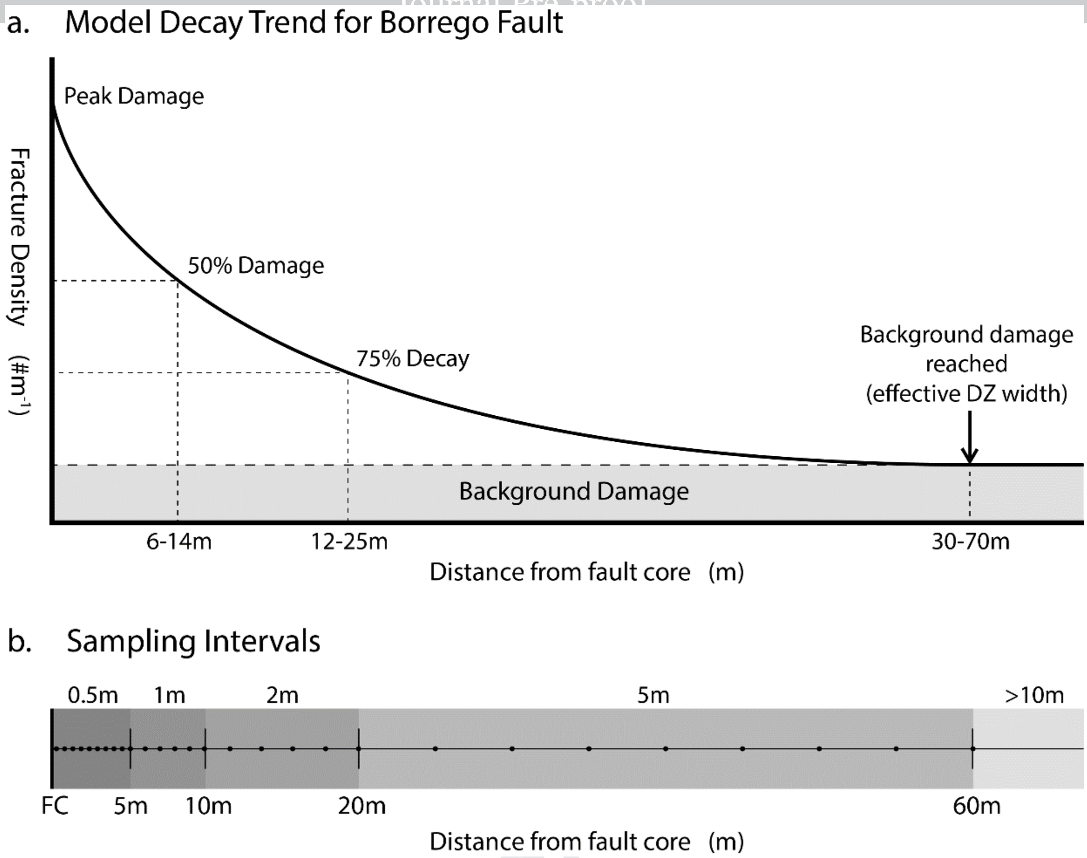

*Figure 5: **a.** A simple approximation of the damage profile in the footwall of the Borrego Fault based on the common models of damage decay, published displacement-DZ width scaling relationships, and a preliminary fault survey to estimate the rough distances shown on the plot. **b.** The resulting design for sample frequency along each transect. Final sample locations are ultimately limited by exposure quality and other field conditions.*

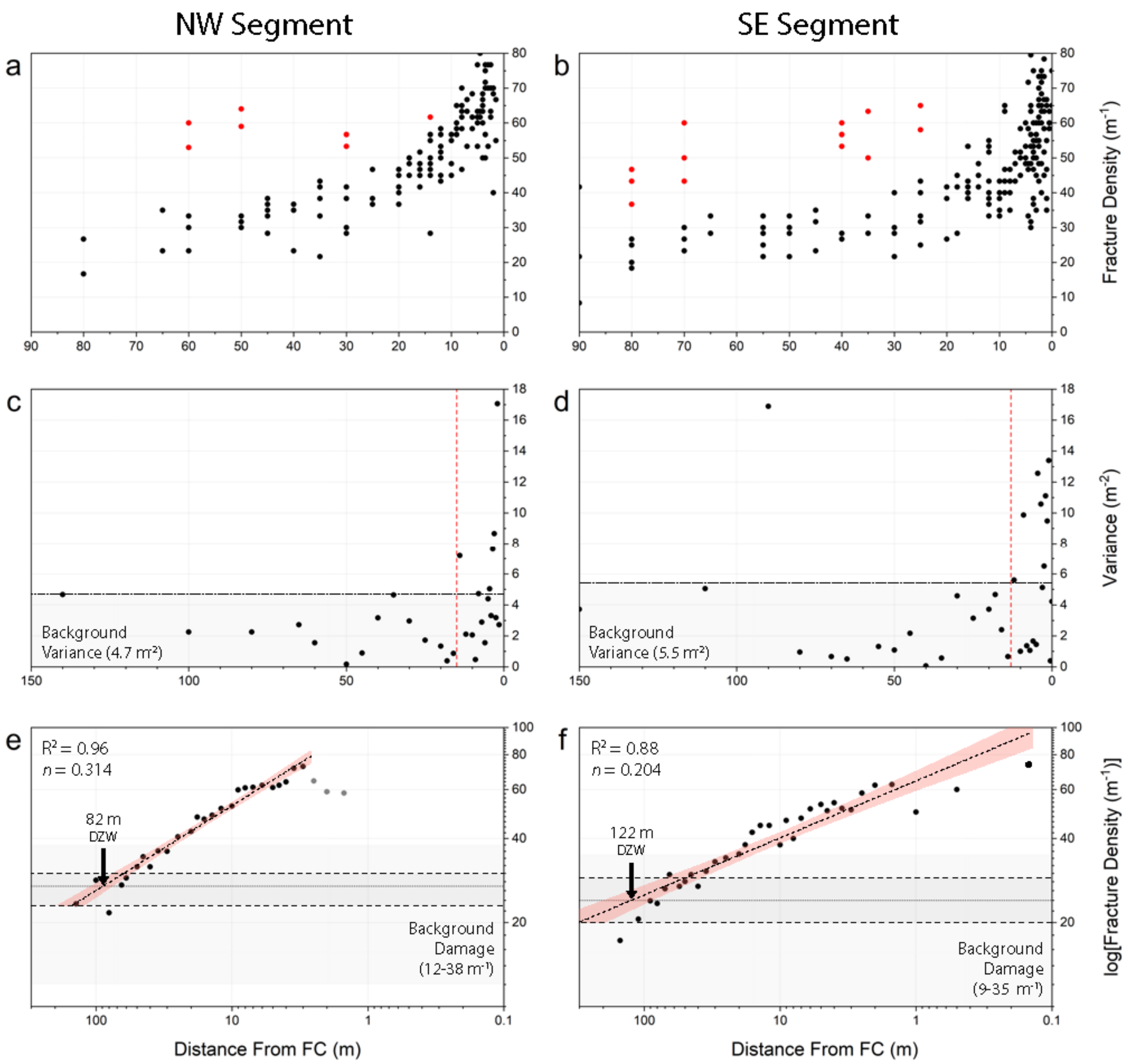

Figure 6: Results of the transect studies along the NW and SE segments of the Borrego Fault. ***a.*** *and* ***b.*** *Scatter plots of all measurements, constrained to 90 m from the fault to better show the wedge-shaped distribution with increased spreading towards the fault core. Measurements influenced by LSF damage are shown in red and removed from subsequent analysis.* ***c.*** *and* ***d.*** *The degree of spreading, quantified by the variance, shows a transition at 13-15 m between an inner zone of high, scattered variance, and an outer zone of low variance at or below the background level. This point is marked on both graphs by the red dashed line.* ***e.*** *and* ***f.*** *The DZW is found using a power law regression on the average fracture density from the 4 transects on each segment. 95% confidence intervals are calculated in R using the standard error. The first three measurements in* ***e.*** *are ignored from the regression due to pulverisation (see main text). n is the slope coefficient.*

Figure 7: (On next page)
a. *Drone image of the 20x5 m pavement, showing the exposed tonalite damage zone and 0.5-1.5 m thick fault core (reddish-brown strip with white lenses). In this image only the first half of the outcrop has been cleaned, which results in a slight paler colour.* ***b.*** *Map of minor subsidiary faults and geological units that make up the fault core (FC) and damage zone on the pavement. The grid outlines the area sampled and imaged for fracture digitisation.* ***c.*** *Digital Fracture Network containing >11,000 fractures manually traced on high resolution images captured on the 4x18 m grid overlain on* ***b.*** ***d.*** *Rose plots of fracture orientations at various distances from the fault showing the rotation and divergence of the main fracture orientation with distance from the fault. The solid red line shows the orientation of the dominant fracture set relative to the main Borrego Fault trace, and the dashed red line (that appears after 9 m) shows the second, possibly conjugate set of fractures.*

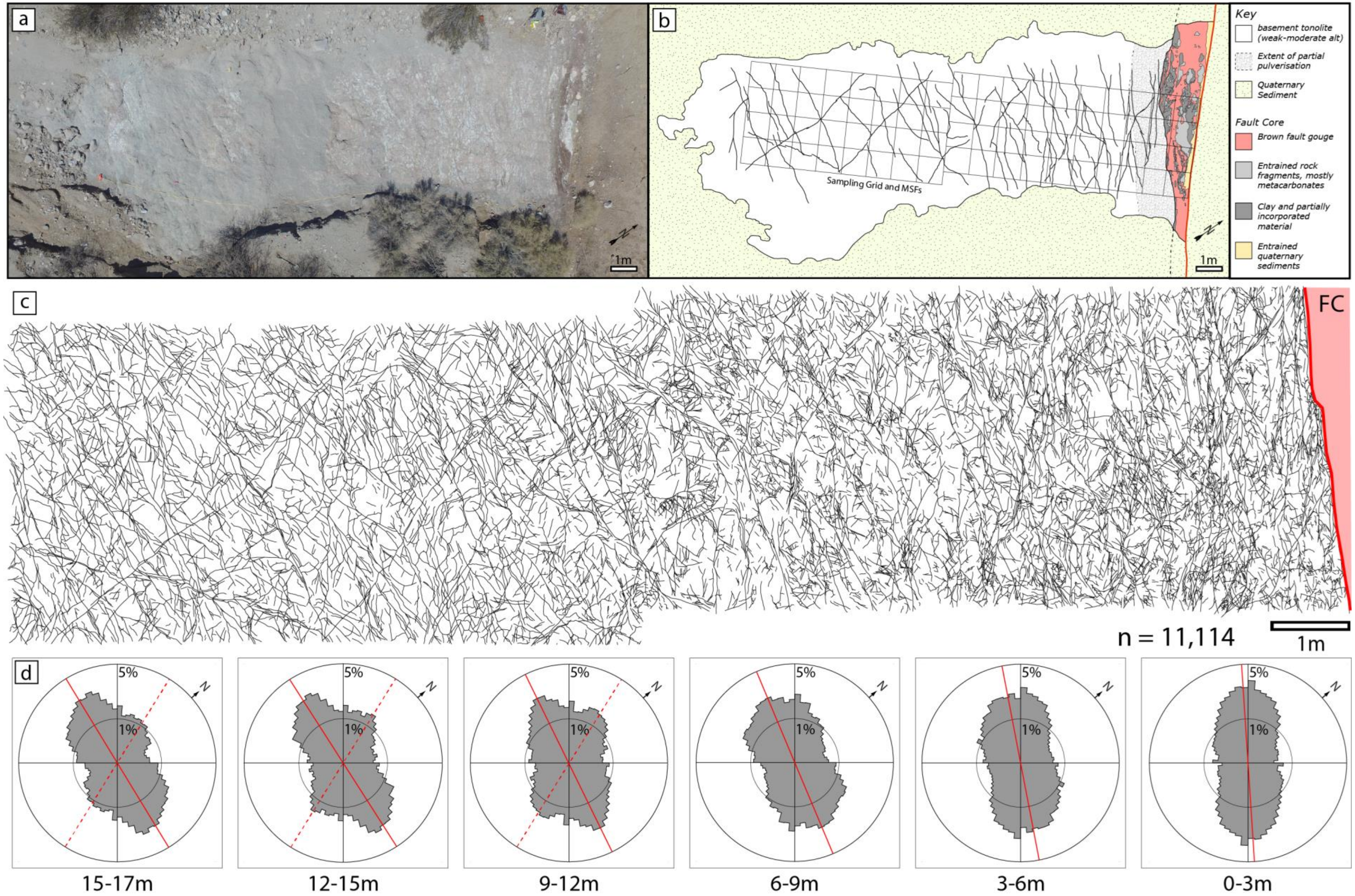
a
1m
b
Sampling Grid and MSFs
1m
Key
basement tonolite (weak-moderate alt)
Extent of partial pulverisation
Quaternary Sediment
Fault Core
Brown fault gouge
Entrained rock fragments, mostly metacarbonates
Clay and partially incorporated material
Entrained quaternary sediments
c
FC
n = 11,114
1m
d
5%
1%
N
15-17m
12-15m
9-12m
6-9m
3-6m
0-3m

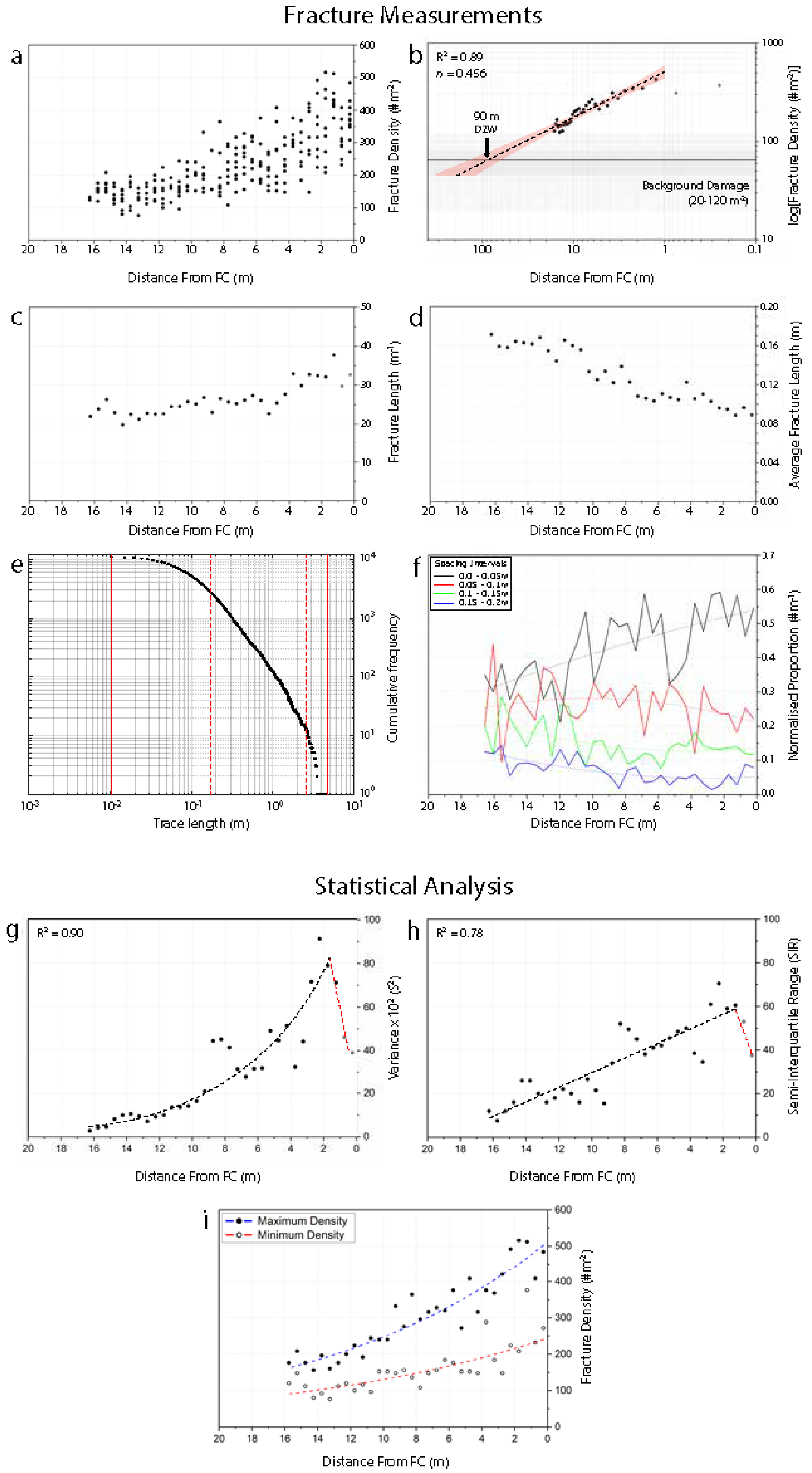

Figure 8: Fracture measurements and statistical analysis of data from the nine 1D pavement transects. ***a.*** *All fracture density measurements from transects T1-T9.* ***b.*** *Average fracture density plot with DZW determined from the power law regression. n is the slope coefficient. 95% confidence intervals generated from standard error in R. Measurements effected by pulverisation shown in grey are ignored from the regression.* ***c.*** *Total fracture length per area vs distance from the fault core. Values are the average of measurements from all nine transects.* ***d.*** *Mean fracture lengths calculated by total fracture length/number of fractures in each 0.5 m bin.* ***e.*** *Cumulative frequency vs fracture length plot for all 11,114 fractures in the digital fracture network. Dashed lines indicate where the data begins to deviate from a power law distribution.* ***f.*** *Distribution of fracture spaces along 34 fault perpendicular scanlines. Fracture spaces have been binned into 5 cm intervals.* ***g.*** *Variance and* ***h.*** *Semi-Interquartile Range, used to quantify the spread of fracture density data around the mean decay trend. A sliding window of 1 m was used to calculate both of these values.* ***i.*** *Maximum and minimum fracture density values at varying distances from the fault core.*

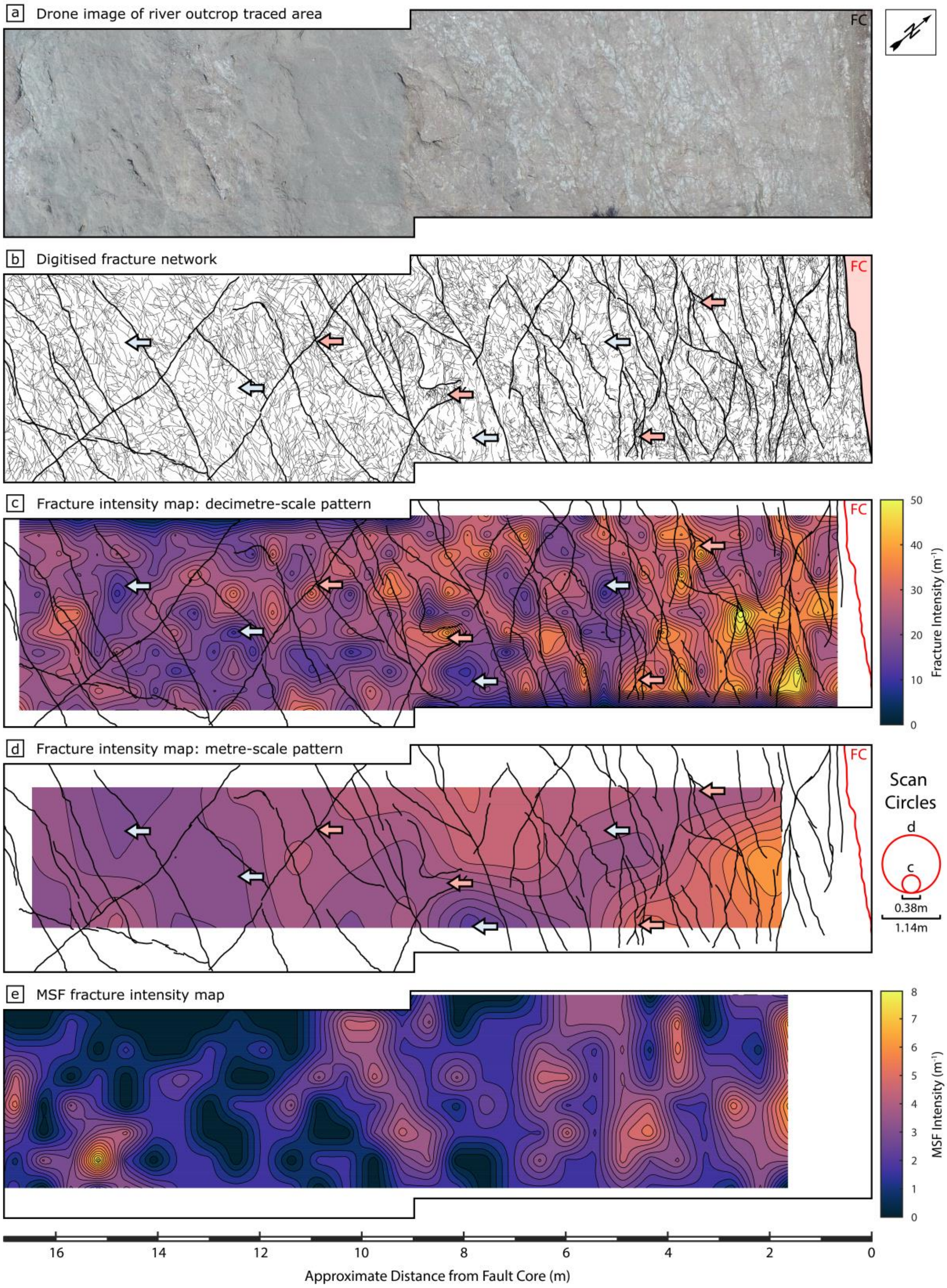

*Figure 9: **a.** Drone image of the platform outcrop, trimmed to the dimensions of the 17x4 m grid. b. Digitised fracture network with minor subsidiary faults highlighted with thicker lines. c. and d. Fracture intensity contour maps of the entire fracture network generated using FracPaQ, with minor subsidiary faults overlain. c. A decimetre-scale pattern emerges when the analysis is performed using a scan circle with diameter between 0.24-0.55 m. High-intensity patches correspond with locations of minor subsidiary faults, notably with fracture tips or the areas where fractures interact (e.g. stepovers, crosscuts, splays, or terminations). Low-intensity patches associate with gaps between minor subsidiary faults or along poorly developed wall damage zones. Some of these points are highlighted with pink (high-intensity) and blue (low-intensity) arrows, and correlate the intensity maps (c/d) with the digitised fracture network (b). d. Large scan circles (>0.8 m diameter) show meter-scale patterns which are discrete from the dm-scale pattern. e. Fracture intensity map of minor subsidiary faults only, showing increasing intensity towards the FC with a high-intensity patch at ~15 m.*

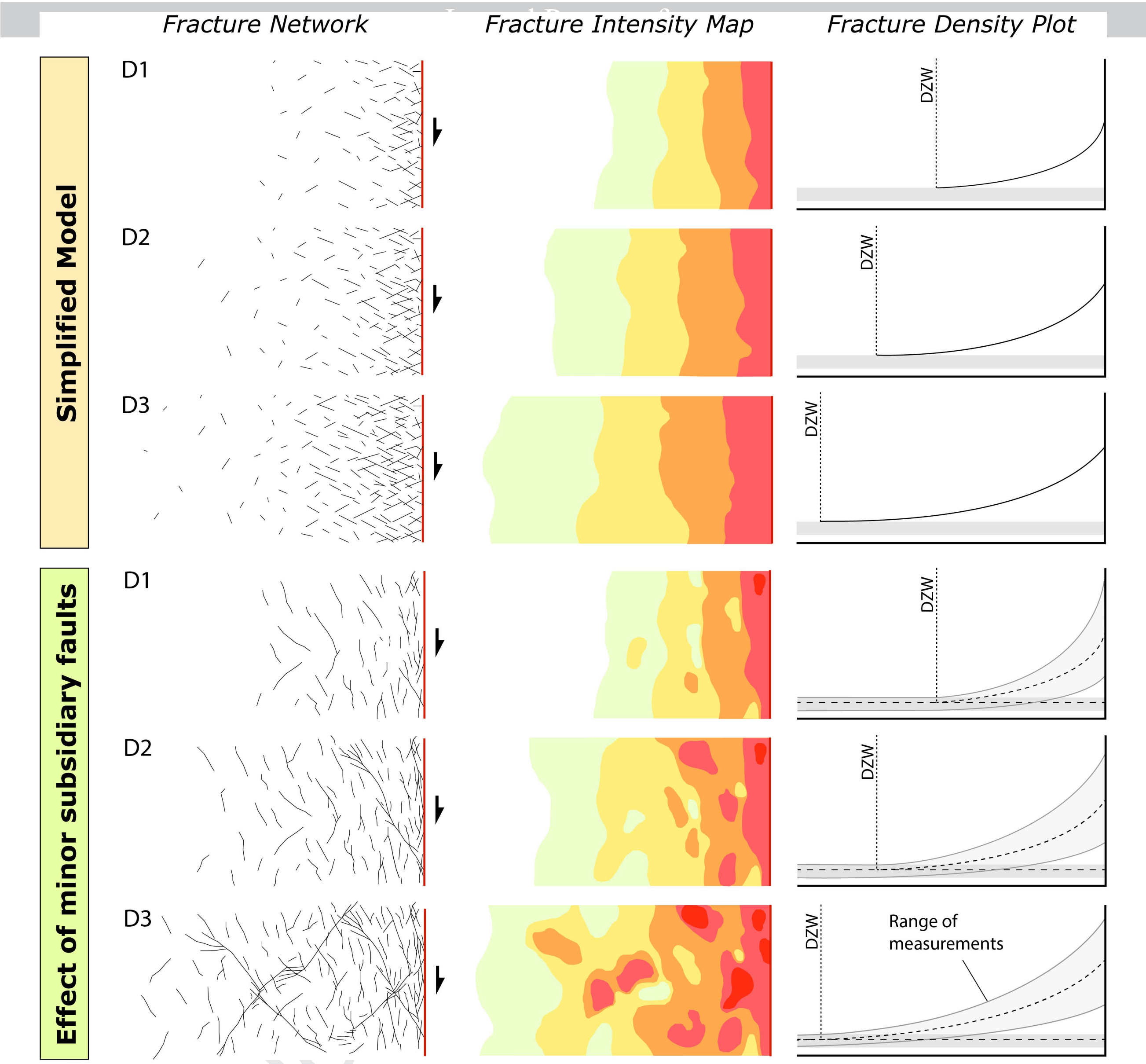

Figure 10: Conceptual models of fracture distribution within the damage zone. A simplified standard damage zone model (above) and a modified model (below), incorporating a patchy fracture intensity distribution and a systematic increase in heterogeneity, defined by an increase in variance, towards the fault core. D1-D3 indicate increasing displacement along the main fault, from an already intermediate stage in D1. The grey cone around the average meso-fracture profile represents the decreasing spread of measurements from a maximum close to the fault core to background levels at a distance less than the damage zone width. High-intensity patches develop in the tip and linking zones of minor subsidiary faults in the damage zone, which increase in frequency as the fault matures. Low-intensity patches occur in blocks bound by minor subsidiary faults and shrink with fault maturity as they are dissected by new faults and/or damage migrates inwards from their edges. Eventually minor subsidiary faults may grow/link to become major subsidiary faults, their own meso-fracture damage zones forming a corridor of increased damage (instead of patches) – not shown in this schematic.

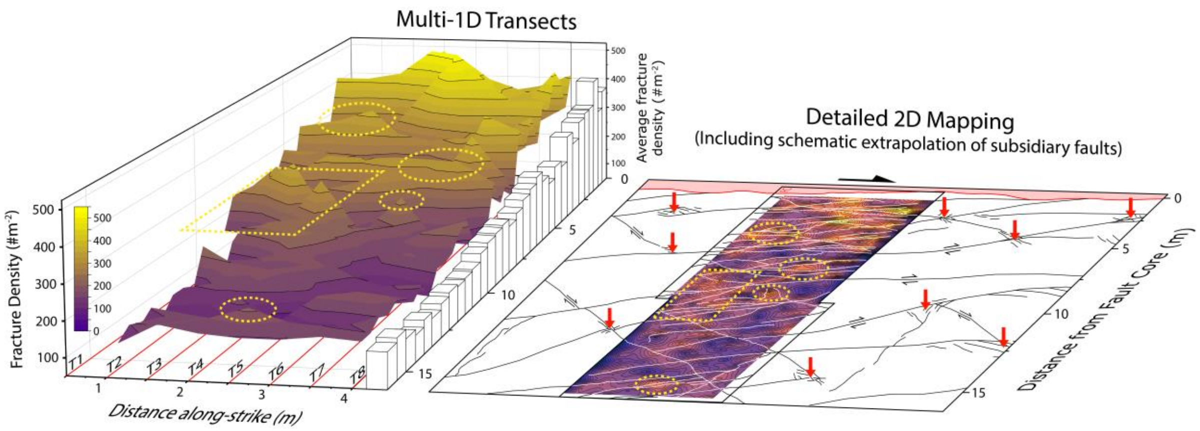

Figure 11: Comparison between the results of a concentrated multi-transect, and detailed 2D fracture mapping study. Similar peaks can be found in both, highlighted by dashed regions, however the 2D fracture intensity map contains a lot more detail that is smoothed in the concentrated multi-transect plot. Faults drawn beyond the 2D fracture intensity map provide a schematic representation of the minor subsidiary fault network extending beyond the outcrop limits. Red arrows highlight zones of increased meso-fracture intensity.

Highlights

- 68 m^2 high-resolution fracture map of 11,114 fractures ranging from cm to m lengths
- Power law decay in fracture density from fault gives a damage zone width of ~85 m
- Heterogeneity in fracture density decreases away from the fault core to ~16 m
- Inner and Outer damage zone defined by increasing heterogeneity from parent rock
- Modified model of fault damage zone evolution explaining the heterogeneity trend

Declaration of interests

☒ The authors declare that they have no known competing financial interests or personal relationships that could have appeared to influence the work reported in this paper.

☐The authors declare the following financial interests/personal relationships which may be considered as potential competing interests: